

Effects from different grades of stickiness between icy and silicate particles on carbon depletion in protoplanetary disks

T. Okamoto^{1,2} and S. Ida¹

¹ Earth-Life Science Institute, Institute of Science Tokyo (previously, Tokyo Institute of Technology), Meguro-ku, 152-8550 Tokyo, Japan

e-mail: okamoto.t.aw@m.titech.ac.jp

² Laboratoire Lagrange, Centre National de la Recherche Scientifique, Observatoire de la Côte d’Azur, 06304 Nice, France

October 30, 2024

ABSTRACT

Context. The Earth and other rocky bodies in the inner Solar System are significantly depleted in carbon, compared to the Sun and the interstellar medium (ISM) dust. Observations suggest that more than half of the carbon material in the ISM and comets are in a highly refractory form, such as amorphous hydrocarbons and (less refractory) complex organics, which can make up the building blocks of rocky bodies. While amorphous hydrocarbons can be destroyed by photolysis and oxidation, previous studies have suggested that the radial transport of solid particles suppresses carbon depletion. The only exception is the case of strictly complex organics as the refractory carbons, which are considerably less refractory than amorphous hydrocarbons.

Aims. We aim to reveal the conditions for the severe carbon depletion in the inner Solar System, by adding potentially more realistic settings: different levels of stickiness between icy and silicate particles and high-temperature regions in the upper optically thin layer of the disk, which were not included in the previous works.

Methods. We performed a 3D Monte Carlo simulation of radial drift and turbulent diffusion of solid particles in a steady accretion disk with the above additional settings as well as ice evaporation and recondensation. We considered the photolysis and oxidation of hydrocarbons in the upper layer as well as the pyrolysis of complex organics to evaluate the radial distribution of carbon fraction in the disk by locally averaging individual particles.

Results. The carbon fraction drops off inside the snow line by two orders of magnitude compared to the solar value, under the following conditions: i) when silicate particles are much less sticky than icy particles and ii) when there are high-temperature regions in the disk upper layer. The former leads to fast decay of the icy pebble flux, while the silicate particles are still piling up inside the snow line. The latter contributes to the efficient turbulent stirring up of silicate particles to the upper UV-exposed layer.

Conclusions. We have identified simulation settings to reproduce a carbon depletion pattern that is consistent with the observed one in the inner Solar System. The conditions are not too restricted and allow for a diverse carbon fraction of rocky bodies. These effects could be responsible for the observed large diversity of metals on photospheres of white dwarfs and may suggest diverse surface environments for rocky planets in habitable zones.

Key words. Protoplanetary disks – meteorites, meteors, meteoroids – Earth – Methods:numerical

Use \titlerunning to supply a shorter title and/or \authorrunning to supply a shorter list of authors.

1. Introduction

The bodies in the Solar System are highly depleted in carbon, compared to the Sun. Figure 1 shows the carbon fraction, f_c , of the Solar System bodies, where the carbon fraction, f_c , is defined by the mass fraction of refractory carbon relative to the total refractory components (for details, see Binkert & Birnstiel 2023). The carbon fractions for the Sun, interstellar medium (ISM) dust, comets, and interplanetary dust particles (IDPs) are calculated from the C/Si atomic ratio in each body (Binkert & Birnstiel 2023). The carbon fractions of chondrite meteorites are calculated using the mass fraction of insoluble carbon contents, normalized by their matrix volume (Alexander et al. 2007, see below). While the f_c values of ISM dust, IDPs, and comets are comparable to the solar value, the f_c values of the bulk silicate Earth (BSE), which is the mantle and crust without the core of the Earth, is lower by 4 orders of magnitudes than the solar value.

The Earth’s mass is not large enough to accrete large amounts of gas. If all carbon carriers are in volatile forms such as CO, CO₂, or CH₄, it is reasonable that carbon components

were not in the Earth’s building blocks (pebbles and planetesimals) near the Earth’s orbit, resulting in the significant carbon depletion in the Earth. However, about half of the carbon carriers in molecular clouds and primordial comets are likely to be in refractory forms. In the ISM, radio spectrographic observations suggest that ~ 60% of the cosmic carbon exists as highly refractory materials including six-membered rings such as amorphous hydrocarbons, polycyclic aromatic hydrocarbons (PAHs), or graphites (Savage & Sembach 1996). They would survive until they arrive at the hot regions with $T \gtrsim 1000$ K where they are destroyed by pyrolysis or oxidation by OH (e.g., Finocchi et al. 1997; Gail & Tieloff 2017). On the other hand, Fomenkova (1997, 1999) argued that about 60% of all solid carbonaceous materials (including less refractory carbon solids) in the comet Halley are “complex organics” such as a mixture of kerogen and insoluble organic matter (IOM) that survive until they are pyrolyzed at $T \sim 500$ K. These organics are often called “refractory organics.” However, because they are much less refractory than amorphous hydrocarbons, graphites, and PAHs, here we refer to them simply as “complex organics” to avoid confusion.

Table 1: Destruction temperature, T_{des} , for each solid carbonaceous component.

Solid carbonaceous component	Process	T_{des} [K]
Amorphous hydrocarbons	Oxidation	$\gtrsim 1100^a$
Graphites	Oxidation	$\gtrsim 1100^a$
PAHs	Oxidation	$> 1000^b$
Volatile organics	Pyrolysis	$\sim 300 - 400^a$
Complex organics	Pyrolysis	$\sim 500^c$

Notes. “Complex organics” refer to mixed organics such as kerogen and insoluble organic matters (IOM), which are often called “refractory organics.” Because they are moderately refractory in this table, we here use “complex organics” to avoid confusion.

^(a) Gail & Trieloff (2017) ^(b) Kress et al. (2010) ^(c) Li et al. (2021)

We summarize the disk mid-plane temperature required for the destruction of each of the refractory carbon materials (T_{des}) in Table 1, which shows that most of the refractory carbon components should be in dust forms around Earth’s orbit. If Earth’s building blocks originated from the same carbon carriers as in molecular clouds, their compositions should be similar to those of ISM dust and comets with the removal of volatile carbon gas that would have been sublimated inside their ice lines. The carbon reduction due to the sublimation of volatile carbon gas should only be on the level of a factor of a few (and certainly not four orders of magnitude).

Assuming that carbon in the Earth’s mantle or crust may have been partitioned to its core in the magma ocean stage (Sakuraba et al. 2021), f_c values of the bulk Earth could be higher by 1 - 2 orders of magnitude than that of BSE. However, even in that case, the Earth is still depleted in carbon by more than two orders of magnitude from the solar value. Remarkably, even carbonaceous chondrites (CC) are depleted in carbon by more than one order of magnitude from the Sun.

The “bulk” values (rather than matrix-normalized values) of f_c for enstatite chondrites (ECs) and ordinary chondrites (OCs) are in between “bulk Earth” and CC, monotonically increasing with the orbital radii of the Earth and the inferred parent asteroids (e.g., Bergin et al. 2015; Binkert & Birnstiel 2023). However, ECs and OCs include substantial chondrules that are carbon-free. The carbons there might have been lost during the flash heating (Gail & Trieloff 2017). It would be more appropriate to normalize the carbon fraction by the matrix volumes (Alexander et al. 2007), as in Fig. 1; the normalized f_c in ECs, OCs, and CC would be similar independent of the heliocentric radius.

These observational data strongly suggest that carbons in the refractory forms should have been destroyed by some mechanism in the inner Solar System. The question of what specific mechanism is at work remains a mystery.

Carbon depletion may have also occurred in many exoplanetary systems. About 25 to 50% of white dwarfs (WDs) are polluted by heavy elements (metals) such as Fe, Si, O, and C in their photospheres (e.g., Zuckerman et al. 2003, 2010; Koester et al. 2014; Hollands et al. 2017); however, these metals should quickly turn to sediment to the WDs’ interiors in the WDs’ strong gravitational fields (Paquette et al. 1986; Koester 2010). This suggests that rocky planets or asteroids fall onto the host WDs through accretion disks (e.g., Okuya et al. 2023, and references therein), implying that the observed metal abundance should reflect the bulk compositions of the rocky bodies and it shows that C/Si is distributed from the solar value down to the BSE value (Zuckerman & Young 2018). The carbon depletion

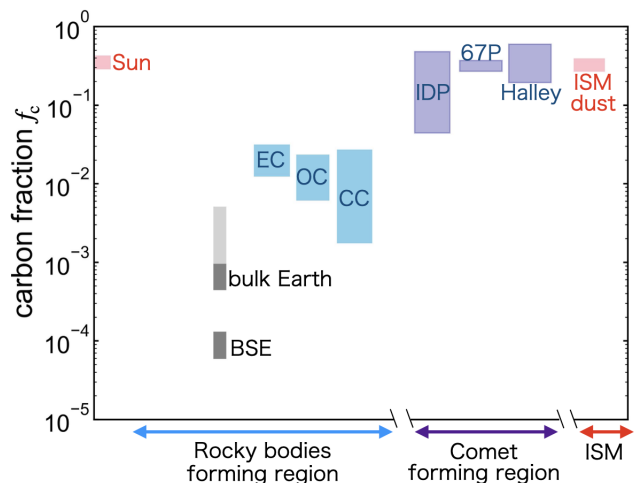


Fig. 1: Carbon fraction of Solar System bodies, where the carbon fraction, f_c , is defined by the mass fraction of carbon in the sum of solid carbon and the silicates. For ISM dust, comets, and IDPs, this fraction is calculated from the C/Si atomic ratio (Matrajt et al. 2005; Bardyn et al. 2017; Bergin et al. 2015; Binkert & Birnstiel 2023, and references therein). For comparison, we also plot the “Sun” values ($f_c \approx 0.25$), which refer to hypothetical dust with solar C/Si. The fractions of chondrites are normalized by the matrix volume of each chondrite (see the main text). While Bergin et al. (2015) and Binkert & Birnstiel (2023) showed f_c fraction monotonically decreases as the decrease in the heliocentric radius decreases, the matrix-normalized f_c of chondrites may be independent of the distance. The uncertainties of chondrites’ f_c values come from the variation among each chondrite. The very low f_c of BSE and “bulk Earth” are also discussed in the main text.

problem is not only an issue in the Solar System but also in exoplanetary systems.

Oxidation destroys amorphous hydrocarbons, PAHs, and graphites. When an oxygen atom collides with dust, a carbon atom is stripped to form a gaseous CO molecule. Lee et al. (2010) showed that enough amounts of hot oxygen atoms to oxidize graphite are produced by far-ultraviolet (FUV) irradiation in an upper layer over the disk photo-surface. The oxidation timescale of graphite is also applied for amorphous hydrocarbons and PAHs. Amorphous hydrocarbons may also be directly destroyed by FUV photons (Anderson et al. 2017); small hydrocarbons are released from the surface of an amorphous hydrocarbon particle that contains 10^6 or more C atoms (Alata et al. 2014, 2015). In this paper, we refer to this destruction as “photolysis.”

The complex organics are thermally destroyed at $T_{\text{des}} \sim 500$ K (Table 1), which we call “pyrolysis.” Although they are converted to gas molecules, half of pyrolysis products may be hydrocarbons with $T_{\text{des}} \gtrsim 1000$ K (e.g., Chyba et al. 1990; Gail & Trieloff 2017). The experiments of Nakano et al. (2003) showed that remnants of pyrolysis can exist even in regions where the temperature exceeds 700 K, although the mass fraction of the remnants is unclear. Bergin et al. (2015) and Li et al. (2021) assumed only complex organics as a source of refractory carbons in ISM to propose that migration of their sublimation line (“soot line”) solves the carbon depletion problem in the inner Solar System. However if the remnants of the pyrolysis are hydrocarbons, the question of how hydrocarbons are destroyed must be discussed, even if the ISM refractory carbons do not include the highly refractory materials: hydrocarbons, PAHs, or graphites.

Klarmann et al. (2018) and Binkert & Birnstiel (2023) studied the carbon depletion in the inner Solar System, through Eulerian diffusion and advection simulations with the two-components fluid approximation of disk gas and dust. Klarmann et al. (2018) calculated the destruction of hydrocarbon particles due to oxidization and FUV photolysis, taking into account the dust drift and diffusion due to disk gas accretion and turbulence. They concluded that it is difficult to explain the observed carbon depletion because the dust radial drift timescale is much shorter than the timescale required to destroy most of the refractory carbon particles there.

Binkert & Birnstiel (2023) considered both the photolysis of amorphous hydrocarbons and pyrolysis of complex organics. They suggested that the carbon depletion could be explained if the FU Ori-type outburst sublimates all of the complex organics and if the dust surface density and the optical depth for FUV are low enough to promote photolysis. However, it is not clear that the FU Ori-type outburst events occurred in the proto-Solar System and enough amount of the irradiated dust particles stay to be building blocks of the inner Solar System bodies. Furthermore, they assumed most of the refractory carbons are complex organics. If their conversion to amorphous hydrocarbons is taken into account, their conclusion may change.

These previous studies assumed that dust is composed only of silicates and carbon materials. However, beyond the snow line, H₂O components are added. Conventional results from experiments and numerical simulations suggested that ice may be stickier than silicate (e.g., Blum & Wurm 2000; Zsom et al. 2011; Wada et al. 2011), and icy particles grow to larger sizes than silicate particles. Here, we assume that carbonaceous solid materials move with silicate particles. If the icy pebbles envelop many small silicate particles, the silicate particles are released by sublimation of the icy mantle. Because of their small size, they are coupled to gas and piled up like traffic jam near the snow line, which may result in rocky planetesimal formation (e.g., Saito & Sirono 2011; Ida & Guillot 2016; Ida et al. 2021) and an enhancement of the crystalline to amorphous ratio of silicates even beyond the snow line (Okamoto & Ida 2022).

These previous studies did not consider the effect of the vertical temperature profile on the particle motions, because they estimated the vertical diffusion timescale by using the mid-plane temperature of the disk. However, in the optically thin upper layer, the local gas temperature is higher than in the mid-plane. It enhances turbulent motions there to lift particles more. At the same time, the lower gas density weakens the gas drag coupling, which suppresses particle stirring. Because oxidation and photolysis are regulated by how much the particles are stirred up to the upper layer, it is important to include the above effects. Our Lagrangian particle tracking method can more easily incorporate these effects than the Eulerian method adopted by the previous studies.

In this paper, we investigate the effect of the different sizes between icy and silicate particles and that of the vertical temperature profile on the carbon depletion problem. We adopt a global 3D Monte Carlo simulation (Ciesla 2010; Okamoto & Ida 2022) to calculate the radial drift and turbulent diffusion motions of solid particles in a disk and the chemical reactions (Ishizaki et al. 2023) such as photolysis in the upper FUV-exposed layer by tracking motions of individual particles. Because our model also calculates the particle size evolution due to coagulation and fragmentation, the pebble flux decay is consistently calculated.

In Sect. 2, we describe our Monte Carlo methods for particle motions and refractory carbon destruction models. In Sect. 3, we show the simulation results. The carbon fraction drops off inside

the snow line by two or more orders of magnitude from the solar value in a fiducial case. We also investigate the dependence on simulation parameters. In Sect. 4, we compare the simulation results to the observational data. Section 5 presents our conclusions.

2. Method

2.1. Disk model

We assumed a self-similar protoplanetary gas disk (Hartmann et al. 1998) with characteristic radius $r_{\text{disk}} = 100$ au. At $r \ll r_{\text{disk}}$, the disk gas accretion rate (\dot{M}_g) is independent of r (steady accretion) and \dot{M}_g decays as $\propto (1 + t/t_{\text{disk}})^{-3/2}$, where $t_{\text{disk}} \approx 10^7(\alpha/10^{-3})^{-1}(r_{\text{disk}}/100 \text{ au})$ yrs. We assumed the conventional gas accretion model due to turbulent diffusion and do not consider disk-wind driven accretion, for simplicity. The gas surface density is given by

$$\begin{aligned} \Sigma_g &= \frac{\dot{M}_g \mu m_{\text{H}} \Omega_{\text{K}}}{3\pi \alpha k_{\text{B}} T_{\text{mid}}} \\ &\approx 1200 \left(\frac{\dot{M}_g}{10^{-8} M_{\odot}/\text{yr}} \right) \left(\frac{\alpha}{10^{-3}} \right)^{-1} \left(\frac{T_{\text{mid}}}{300 \text{ K}} \right)^{-1} \left(\frac{r}{1 \text{ au}} \right)^{-3/2} \text{ g/cm}^2, \end{aligned} \quad (1)$$

where α is a parameter of turbulent strength and Ω_{K} is Keplerian frequency.

The hydrostatic local gas density is given by

$$\rho_g = \frac{\Sigma_g}{\sqrt{2\pi} H_g} \exp\left(-\frac{z^2}{2H_g^2}\right), \quad (2)$$

where H_g is the disk gas scale height. The disk aspect ratio is

$$h_g = \frac{H_g}{r} = 0.034 \left(\frac{T}{300 \text{ K}} \right)^{1/2} \left(\frac{r}{1 \text{ au}} \right)^{1/2}. \quad (3)$$

We set the gas disk temperature distribution as follows. We calculate the mid-plane temperature T_{mid} by $T_{\text{mid}}^4 = T_{\text{vis}}^4 + T_{\text{irr}}^4$, where T_{vis} and T_{irr} are the temperature determined by viscous heating and irradiation, respectively. The viscous heating temperature with the opacity given by Bell & Lin (1994): $T_{\text{vis}} = \min(T_{\text{vis,ice}}, \max(T_{\text{vis,eva}}, T_{\text{vis,sil}}))$, where $T_{\text{vis,ice}}$ and $T_{\text{vis,sil}}$ are the temperatures with ice and silicate dust opacity, respectively, and $T_{\text{vis,eva}}$ is that with the opacity for a transition from ice to silicate due to the evaporation of ice, which are given by

$$T_{\text{vis,ice}} = 1141 \left(\frac{\dot{M}_g}{10^{-8} M_{\odot}/\text{yr}} \right)^{2/3} \left(\frac{\alpha}{10^{-3}} \right)^{-1/3} \left(\frac{r}{1 \text{ au}} \right)^{-3/2} \text{ K}. \quad (4)$$

$$T_{\text{vis,eva}} = 270 \left(\frac{\dot{M}_g}{10^{-8} M_{\odot}/\text{yr}} \right)^{1/6} \left(\frac{\alpha}{10^{-3}} \right)^{-1/12} \left(\frac{r}{1 \text{ au}} \right)^{-3/8} \text{ K}, \quad (5)$$

$$T_{\text{vis,sil}} = 433 \left(\frac{\dot{M}_g}{10^{-8} M_{\odot}/\text{yr}} \right)^{4/9} \left(\frac{\alpha}{10^{-3}} \right)^{-2/9} \left(\frac{r}{1 \text{ au}} \right)^{-1} \text{ K}. \quad (6)$$

On the other hand, the temperature by irradiation is set to (Okamoto et al. 2011; Ida et al. 2016)

$$T_{\text{irr}} = 150 \left(\frac{r}{1 \text{ au}} \right)^{-3/7} \text{ K}. \quad (7)$$

The transition between T_{vis} and T_{irr} occurs at

$$r_{\text{vis-irr}} = 6.6 \left(\frac{\dot{M}_g}{10^{-8} M_{\odot}/\text{yr}} \right)^{28/45} \left(\frac{\alpha}{10^{-3}} \right)^{-14/45} \text{ au}. \quad (8)$$

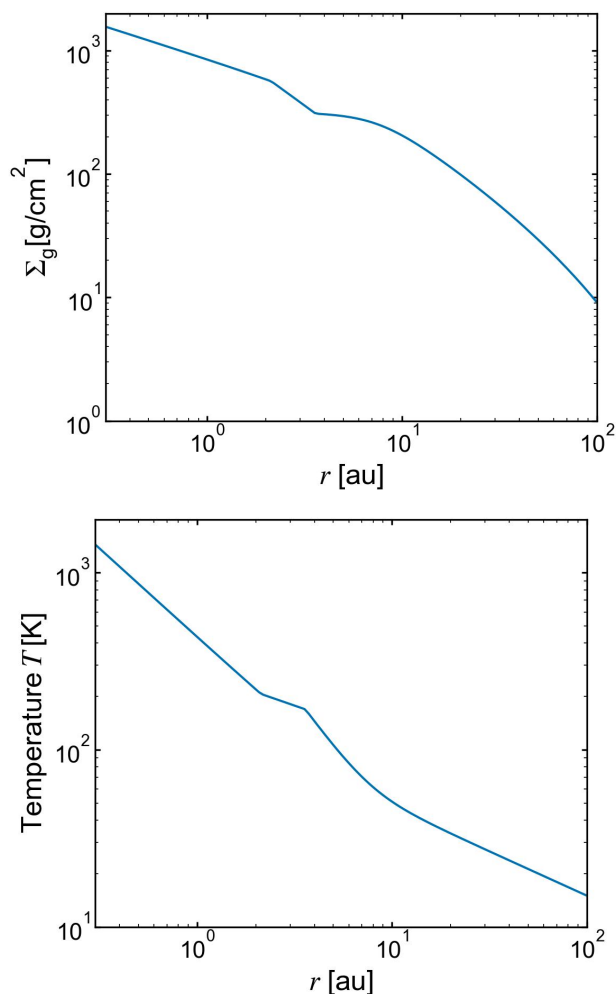


Fig. 2: Gas surface density, Σ_g , (upper panel) and the mid-plane temperature (lower panel) in the fiducial run.

Figure 2 shows the gas surface density and the mid-plane temperature distributions in the fiducial run.

The vertical temperature distribution is set as follows. In the upper optically thin FUV-exposed layer (at $|z| \gtrsim (3-4) H_g$), the temperature is generally higher than near the mid-plane, which is given by (Klarmann et al. 2018)

$$T_{\text{FUV}} = 750 \left(\frac{r}{1 \text{ au}} \right)^{-3/5} \text{ K}. \quad (9)$$

We connect T_{FUV} with T_{mid} in the mid-plane as

$$T_z^4 = T_{\text{mid}}^4 (1 - \exp(-\tau_{\text{FUV},z})) + T_{\text{FUV}}^4 \exp(-\tau_{\text{FUV},z}), \quad (10)$$

where $\tau_{\text{FUV},z}$ is the vertical optical depth for FUV given by Eq. (44). Figure 3 shows T_z at 1 au.

2.2. Monte Carlo simulation

2.2.1. Representative refractory carbons

We considered the two types of refractory carbons: amorphous hydrocarbon as the highly refractory materials and complex organics as modest refractory materials, although, in many simulation sets, we considered only amorphous hydrocarbons by the reason in Sect. 1. Because graphites and PAHs would have similar destruction temperatures (Table 1) and, in an observational sense, it is not clear what fraction of interstellar carbon exists

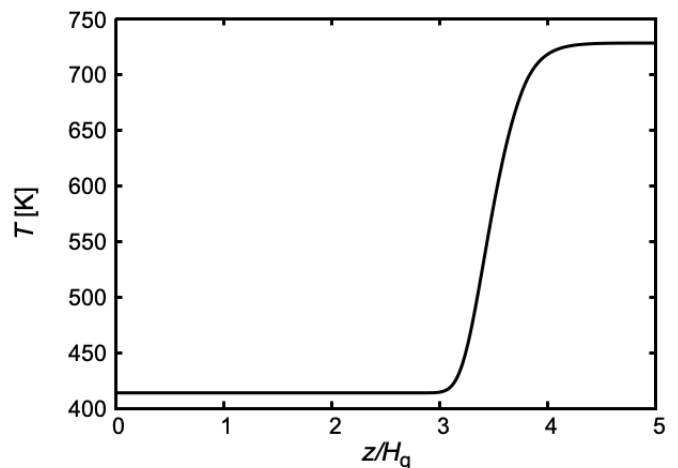


Fig. 3: Vertical temperature profile at 1 au given by Eq. (10).

in individual forms of refractory materials, the highly refractory carbons are represented by the amorphous hydrocarbons (in this paper). We assumed that amorphous hydrocarbon particles are destructed by the photolysis and/or oxidation in the FUV-exposed layer.

2.2.2. Photolysis and oxidation

When the carbonaceous particles are lifted to the upper layer by turbulence, the particles are assumed to be “photodegraded” or “oxidized.” In this paper, “photolysis” is defined as the reaction that small hydrocarbon volatile molecules such as methane are released from the surface of the amorphous hydrocarbon particles by FUV, as suggested by Alata et al. (2015), and “oxidation” means the reaction that single C atoms are removed from the carbon particle surface by the collisions with oxygen atoms as gaseous carbon monoxide molecules. Since the oxygen atoms should be abundant only in the upper layer of the disk (e.g., Lee et al. 2010), we calculated the oxidation rate only when the particle exists in the FUV-exposed layer (see Sect. 2.4.1). Although oxidation by OH could occur (e.g., Bauer et al. 1997; Finocchi et al. 1997), the abundance of OH is uncertain near the mid-plane and the oxygen atoms are more abundant than OH in the FUV-exposed layer (Lee et al. 2010). Accordingly, we did not consider oxidation by OH. The rates of photolysis and oxidation are described in Sects. 2.4.2 and 2.4.3.

When the Stokes number (St), which is defined by the stopping time due to gas drag scaled by the inverse of local Kepler frequency, is smaller than the viscosity parameter α for the released and piled-up silicate particles at the snow line (and when $\text{St} > \alpha$ for icy pebbles), the silicate particles are stirred up more highly than the icy pebbles. In this case, the piled-up silicate particles block FUV radiation from the central star to the region beyond the snow line, which is also known as the “shadow area” (e.g., Ueda et al. 2019; Ohno & Ueda 2021). Therefore, we assumed that amorphous hydrocarbons are not destroyed outside the snow line.

2.2.3. Fragmentation limit velocity

In the fiducial case, we adopted the conventional fragmentation limit velocity for ice particles as $v_{\text{frag,ice}} = 10 \text{ m/s}$ (e.g., Wada et al. 2013; Gundlach & Blum 2015) and for silicate particles as $v_{\text{frag,sil}} = 1 \text{ m/s}$ (e.g., Wada et al. 2013). We note that this conven-

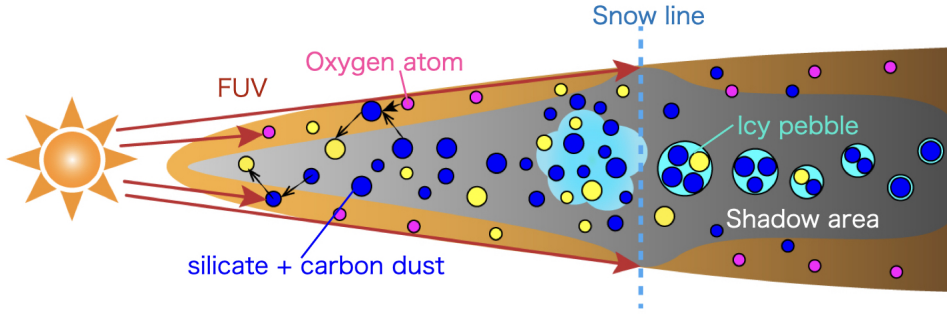


Fig. 4: Overview of our models for gas disk and particle evolution in different disk regions. The blue and yellow particles represent silicates with and without refractory carbon. The light blue particles represent icy pebbles. The pink particles show the oxygen atoms that are formed by the destruction of oxygen molecules because of the FUV radiation which is described as red arrows. The light blue dashed line is the snow line. Icy pebbles enclosing many small silicates drift to the snow line (blue dashed line) from the outer region. Orange upper and lower layers are FUV-exposed regions, where oxygen atoms exist.

tional notion is now challenged by new experiments and recent observations of the protoplanetary disks (see below). In this fiducial case, silicate particles cannot grow enough and stay small. We assumed that amorphous hydrocarbons are included in the silicate particles. Outside the snow line, water vapor condenses on the small silicate particles and these ice-enveloped particles would stick together according to the larger fragmentation velocity for ice to form relatively large aggregates, known as "icy pebbles." When the particles pass inward the snow line, the icy mantle evaporates, and the small silicate particles inside the icy pebbles are released. As we will show later, the released silicate particles are piled up because they are coupled more strongly to disk gas than the icy pebbles are. The sizes of the silicate particles and the icy pebbles are calculated automatically by the model considering the fragmentation limit (Sect. 2.2.5).

Realistic fragmentation velocities of the icy and silicate particles remain uncertain. As mentioned above, although the previous studies showed that icy particles can stick easier than silicates, recent experiments showed that the stickiness of icy particles is similar to that of silicates (e.g., Musiolik & Wurm 2019; Schr apler et al. 2022). Furthermore, recent observations could also show that the size of mass-dominant icy particles is $\lesssim 1$ mm in outer regions of protoplanetary disks, which corresponds to the fragmentation velocity of icy particles of $\lesssim 1$ m/s (Kataoka et al. 2015; Ueda et al. 2024). However, even if the fragmentation velocities of silicate and icy particles are similar to each other, the icy particles could become larger by recondensation of water vapor near the snow line (Ros et al. 2019), which is not incorporated in this study. In this case, the results can be similar to the fiducial case. A more detailed investigation is left for future work.

We set the fragmentation limit velocities for amorphous hydrocarbons to be the same as silicate particles to highlight the effect of the fragmentation velocity difference, for simplicity. We note that the stickiness of carbonaceous materials is also unclear. Although some previous studies suggested complex organics on the particle's surface make the silicate particle stickier (e.g., Kudo et al. 2002; Homma et al. 2019), a recent experiment showed that their stickiness is similar to dry silica dust (Bischoff et al. 2020).

2.2.4. Orbital evolution of particles

In order to follow the orbital evolution of silicate particles described in Sect. 2.2.3, we employed the 3D Monte Carlo simulation method for radial drift and diffusion of silicate particles

developed by Ciesla (2010, 2011). The surface density evolution of the icy and silicate particles is determined by the concentration equation:

$$\frac{\partial \Sigma_d}{\partial t} = \frac{1}{r} \frac{\partial}{\partial r} \left[r \Sigma_d \left(v_r - \frac{D}{\Sigma_d / \Sigma_g} \frac{\partial}{\partial r} \left(\frac{\Sigma_d}{\Sigma_g} \right) \right) \right], \quad (11)$$

where Σ_d is the surface density of the icy and silicate particles, D is their diffusivity, and v_r is their radial drift velocity. The vertical advection-diffusion equation is given by

$$\frac{\partial \rho_d}{\partial t} = \frac{\partial}{\partial z} \left(\rho_g D \frac{\partial}{\partial z} \left(\frac{\rho_d}{\rho_g} \right) \right) - \frac{\partial}{\partial z} (\rho_d v_z), \quad (12)$$

where ρ_d is the local spatial density of solid particles. In a steady accretion disk, the changes in the positions in Cartesian coordinates (x, y, z) of each particle after the timestep δt are given by

$$\delta x = v_r \times \frac{x}{r} \delta t + \mathcal{R}_x \sqrt{6D(x') \delta t}, \quad (13)$$

$$\delta y = v_r \times \frac{y}{r} \delta t + \mathcal{R}_y \sqrt{6D(y') \delta t}, \quad (14)$$

$$\delta z = \left[v_z + \frac{1}{\rho_g} \frac{\partial (D \rho_g)}{\partial z} \right] \delta t + \mathcal{R}_z \sqrt{6D(z') \delta t}, \quad (15)$$

where δt is given by the inverse of the local Keplerian frequency, $\delta t = \Omega_K^{-1}$, and x' , y' , and z' are given by

$$x' = x + \frac{1}{2} \frac{\partial D}{\partial x} \delta t; \quad y' = y + \frac{1}{2} \frac{\partial D}{\partial y} \delta t; \quad z' = z + \frac{1}{2} \frac{\partial D}{\partial z} \delta t. \quad (16)$$

The first and second terms on the right-hand sides represent the advection and diffusion. In the diffusion terms, \mathcal{R}_x , \mathcal{R}_y , and \mathcal{R}_z are independent random numbers in a range of $[-1, 1]$ with a root mean square of $1/\sqrt{3}$. We set the particles' diffusivity considering collective effect as (Hyodo et al. 2021; Okuya et al. 2023)

$$D = \frac{\Lambda}{1 + \Lambda^2 \text{St}^2} \nu, \quad (17)$$

where ν is the gas turbulent viscosity given by

$$\nu = \alpha h_g^2 r^2 \Omega_K, \quad (18)$$

and St is the Stokes number given by

$$\text{St} = \begin{cases} \frac{\rho_{\text{bulk}} s}{\rho_g v_{\text{th}}} \Omega_K & \left[s \leq \frac{9}{4} \lambda_{\text{mfp}} : \text{Epstein} \right], \\ \frac{\rho_{\text{bulk}} s}{\rho_g v_{\text{th}}} \frac{4s}{9 \lambda_{\text{mfp}}} \Omega_K & \left[s \geq \frac{9}{4} \lambda_{\text{mfp}} : \text{Stokes} \right], \end{cases} \quad (19)$$

where $v_{\text{th}} = \sqrt{8/\pi} c_s$, c_s is the sound speed of gas, λ_{mfp} is the mean free path of gas, $\Lambda = (1 + \rho_d/\rho_g)^{-1}$, and ρ_{bulk} is the bulk density of the particle, which is assumed to be 3.0 g/cm^3 for the silicate particles and 1.5 g/cm^3 for icy pebbles.

Because we have adopted a disk temperature model where T is raised at $|z| \gtrsim$ a few H_g (Fig. 4), we chose to adopt a vertical diffusivity that is calculated by local temperature. On the other hand, because most of the particles should be within the gas scale height, we set the radial diffusivity calculated by the mid-plane temperature without a vertical dependency. In this case, the radial dependence of diffusivity can be neglected in Eq. (16). In contrast, D can change significantly for $z \rightarrow z'$ due to the steep increase or decrease of the temperature, as shown in Fig. 3. Thus, we can assume $D(x') \sim D(x)$ and $D(y') \sim D(y)$.

The radial drift velocity due to gas drag is given by (Ida & Guillot 2016; Schoonenberg & Ormel 2017)

$$v_r \simeq -\frac{\Lambda}{1 + \Lambda^2 \text{St}^2} (2\Lambda \text{St} \eta v_K + u_v), \quad (20)$$

where v_K is the local Keplerian velocity, u_v is the disk gas (inward) accretion velocity given by $u_v = 3\nu/2r = (3\alpha h_g^2/2)v_K$, and η is the degree of deviation of the gas rotation angular velocity Ω from the Keplerian one, given by

$$\eta \equiv \frac{\Omega_K - \Omega}{\Omega_K} = -\frac{1}{2} \frac{d \ln P}{d \ln r} h_g^2 = C_\eta h_g^2. \quad (21)$$

For simplicity, we take $C_\eta = 11/8$ for $T \propto r^{-1/2}$. The vertical advection velocity v_z is given by (Ciesla 2010):

$$v_z = -\frac{\text{St}}{1 + \text{St}} \Omega z. \quad (22)$$

Therefore, Eqs. (13) to (15) can be rewritten as

$$\delta x = -\frac{\Lambda}{1 + \Lambda^2 \text{St}^2} \left[2\Lambda C_\eta \text{St} + \frac{3}{2} \alpha \right] h_g^2 x + \mathcal{R}_x \sqrt{\frac{6\alpha\Lambda}{1 + \Lambda^2 \text{St}^2}} h_g r, \quad (23)$$

$$\delta y = -\frac{\Lambda}{1 + \Lambda^2 \text{St}^2} \left[2\Lambda C_\eta \text{St} + \frac{3}{2} \alpha \right] h_g^2 y + \mathcal{R}_y \sqrt{\frac{6\alpha\Lambda}{1 + \Lambda^2 \text{St}^2}} h_g r, \quad (24)$$

$$\delta z = -\left(\frac{\text{St}}{1 + \text{St}} + \alpha \right) z + \mathcal{R}_z \sqrt{\frac{6\alpha\Lambda}{1 + \Lambda^2 \text{St}^2}} h_g(z') r. \quad (25)$$

In our simulation, at every timestep, we calculated the instantaneous surface and local densities of solids (icy and silicate particles) from the super-particle distribution to evaluate size growth and collective effect. The solid surface density at r is given with the number of super-particles, ΔN_r , in the radial width of Δr around r given by

$$\Sigma_d = \frac{m \Delta N_r}{2\pi r \Delta r} = \frac{m \Delta N_r}{2\pi r^2 \times 2.3(\Delta \log_{10} r)}. \quad (26)$$

where m is the super-particle mass. The solid local density at r and z is calculated by the number of super-particles $\Delta N_{r,z}$ in the radial and vertical width of Δr and Δz , given by

$$\rho_d = \frac{m \Delta N_{r,z}}{2\pi r \Delta r \times 2\Delta z} = \frac{m \Delta N_{r,z}}{4\pi r^2 \times 2.3(\Delta \log_{10} r) \Delta z}. \quad (27)$$

When the initial state of the surface density of particles is given by $\Sigma_d = Z_0 \Sigma_g$, the initial number of particles in each cell

Table 2: Parameters we use in this paper.

Quantity	Symbol	Value
Stellar FUV luminosity [L_\odot]	L_{FUV}	0.01
Gas accretion rate [M_\odot/yr]	\dot{M}_g	10^{-9} , 10^{-8}
Turbulence strength	α	5×10^{-4} , 10^{-3}
Disk radius [au]	r_{disk}	100
Initial solid-to-gas ratio	Z_0	0.01 , 0.05
Fragmentation velocity for ice [m/s]	$v_{\text{frag,ice}}$	1, 10
Fragmentation velocity for silicate [m/s]	$v_{\text{frag,sil}}$	0.1, 1 , 10

Notes. The bold letters show the parameters of the fiducial run.

$\Delta N_{r,0}$ is given by

$$\begin{aligned} \Delta N_{r,0} &= \frac{Z_0 \Sigma_g \times 4.6\pi r^2 (\Delta \log_{10} r)}{m} \\ &\simeq 81 \left(\frac{Z_0}{0.01} \right) \left(\frac{\Delta \log_{10} r}{0.05} \right) \left(\frac{\Sigma_g}{1000 \text{ g/cm}^2} \right) \left(\frac{m}{10^{-8} M_\odot} \right)^{-1} \left(\frac{r}{1 \text{ au}} \right)^2. \end{aligned} \quad (28)$$

We summarize the simulation parameters in Table 2.

2.2.5. Size evolution of particles

We used a super-particle approximation. One super-particle represents a huge number of small dust particles. We assigned a single dust size to each super-particle that has the same total mass. We calculated the particle size growth by the ‘‘two population model’’ developed by Birnstiel et al. (2012). The size of the large super-particle is given by

$$s(t + \delta t) = \min [s_{\text{max}}, s(t) \exp(Z\Omega_K \delta t)], \quad (30)$$

where

$$s_{\text{max}} = \min(s_{\text{frag}}, s_{\text{drift}}), \quad (31)$$

which is the local maximum size at the mid-plane corresponding to the Stokes numbers (Eq. (19)) and s_{frag} and s_{drift} are the limits by fragmentation and radial drift, given by

$$\text{St}_{\text{frag}} = 0.37 \frac{v_{\text{frag}}^2}{3\alpha c_s^2} \simeq 2.3 \times 10^{-2} \left(\frac{v_{\text{frag}}}{10 \text{ m/s}} \right)^2 \left(\frac{\alpha}{10^{-3}} \right)^{-1} \left(\frac{T}{150 \text{ K}} \right)^{-1}, \quad (32)$$

$$\text{St}_{\text{drift}} = 0.40 \frac{\Sigma_d}{\Sigma_g C_\eta} \left(\frac{r\Omega_K}{c_s} \right)^2 \simeq 0.49 \left(\frac{\Sigma_d/\Sigma_g}{10^{-3}} \right) \left(\frac{r}{1 \text{ au}} \right)^{-1} \left(\frac{T}{150 \text{ K}} \right)^{-1}. \quad (33)$$

We set $\rho_{\text{bulk}} = 3.0 \text{ g/cm}^3$ inside the snow line and $\rho_{\text{bulk}} = 1.5 \text{ g/cm}^3$ outside the snow line.

When s of a super-particle exceeds s_{frag} , we assume that a collision occurs with $v > v_{\text{frag}}$ and randomly chose a new representative particle size by the weight of $dN(s) \propto s^{-3.5} ds$, where $N(s)$ is a cumulative size distribution function, with the maximum and minimum sizes of s_{frag} and $0.1 \mu\text{m}$, conserving the mass of the super-particle. The minimum size is fixed, while s_{frag} is updated at every timestep.

2.3. Evaporation and recondensation of ice

We consider the evaporation and recondensation of icy particles, following Ciesla & Cuzzi (2006). The decrease rate of the particle mass (m_p) is given by a balance between recondensation and

evaporation as (Lichtenegger & Komle 1991)

$$\frac{dm_p}{dt} = 4\pi s^2 v_{th} (\rho_{eq} - \rho_{vap}) = 2s^2 v_{th}^{-1} (P_{eq} - P_{vap}), \quad (34)$$

where $\rho_{vap} = \Sigma_{vap} / \sqrt{2\pi} H_g$ is the vapor density, the averaged normal component of the velocity passing through the particle surface v_{th} is given by

$$v_{th} = \frac{c_s}{\sqrt{2\pi}} = \frac{1}{\sqrt{2\pi}} \left(\frac{k_B T}{\mu_{H_2O}} \right)^{1/2}, \quad (35)$$

with μ_{H_2O} being the molecular weight of water and we used

$$P_{vap} = \rho_{vap} c_s^2. \quad (36)$$

The equilibrium pressure P_{eq} is given by the Clausius-Clapeyron equation (Lichtenegger & Komle 1991):

$$P_{eq} = 1.14 \times 10^{13} \cdot \exp\left(-\frac{6062 \text{ K}}{T}\right) \text{ g cm}^{-1} \text{ s}^{-2}. \quad (37)$$

For each super-particle, P_{eq} and P_{vap} at the location of the particle are calculated at each timestep. When $P_{eq} > P_{vap}$, the evaporation probability during δt is evaluated as

$$p_{evp} = \min\left(\frac{\dot{m}_p \delta t}{m_p}, 1\right) = \min\left(\frac{2}{v_{th}} \frac{3}{4\pi \rho_{bulk} s} (P_{eq} - P_{vap}) \delta t, 1\right). \quad (38)$$

For a generated random number \mathcal{R} in $[0, 1]$, if $\mathcal{R} \leq p_{evp}$, we regard that the icy super-particle evaporates.

When $P_{eq} < P_{vap}$, recondensation should occur immediately. The change in the water vapor surface density, $\Delta \Sigma_{vap}$, should be corresponding to $P_{vap} - P_{eq}$. The recondensation probability is evaluated as

$$p_{cnd} = \min\left(\frac{\Delta \Sigma_{vap}}{\Sigma_{vap}}, 1\right) = \min\left(\frac{P_{vap} - P_{eq}}{P_{vap}}, 1\right). \quad (39)$$

Similarly, the icy super-particle condenses if $\mathcal{R} \leq p_{cnd}$ for a newly generated \mathcal{R} .

We assume water vapor re-condenses on surfaces of both ice and silicate dust particles. Ros et al. (2019) suggested water vapor tends to re-condense on the icy pebbles' surface rather than the silicate dust surface. Even if we restrict recondensation to silicate particle surfaces, our results hardly change.

In this paper, we define the ‘‘snow line’’ as the radius where the mass fraction of H_2O ice exceeds 1% of total solid mass. In the fiducial case, the snow line radius is $r_{snow} \simeq 3.7$ au. We assume that smaller silicate particles are released after an icy particle passes the snow line. Even if fluffy silicate aggregates are first formed as icy mantle evaporates (Aumatell & Wurm 2011), we assume that they are destroyed by collisional fragmentation into grains, for simplicity.

2.4. Carbon destruction rate by FUV

Alata et al. (2014, 2015) suggested that hydrocarbon molecular gas is released from the surface of amorphous hydrocarbons by FUV. They are suggested to exist in the ISM and comets as so-called ‘‘amorphous carbons.’’

We calculated the carbon fraction change with the carbon depletion timescale:

$$\delta f_c = -2 \left(\frac{\delta t}{t_{ph}} + \frac{\delta t}{t_{ox}} \right) f_c, \quad (40)$$

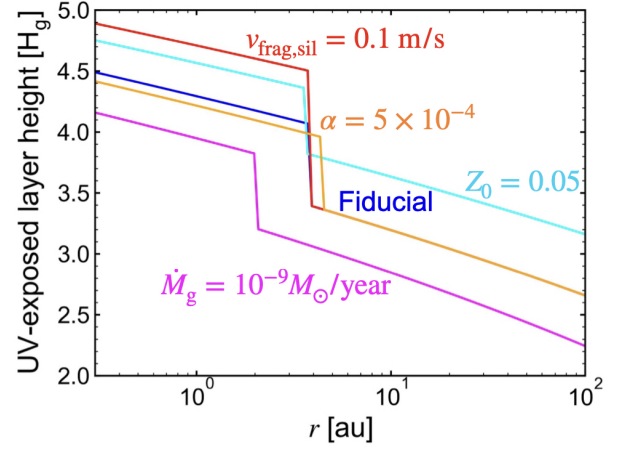


Fig. 5: Height of the FUV-exposed layer for the initial condition.

where t_{ph} and t_{ox} are timescale of photolysis and oxidation. To suppress a too abrupt change of the carbon fraction, when $|\delta f_c / f_c| \geq 0.01$ with a dynamical timestep, we adopted a shorter chemical timestep δt_{chem} , such that $|\delta f_c / f_c| < 0.01$. We then recalculated the timescale by updating the particle’s position, assuming that the particle moves linearly during the dynamical timestep δt (Ishizaki et al. 2023). The detailed calculation model is shown in Appendix A.

2.4.1. Opacity for FUV

The vertical optical depth ($\tau_{z,\lambda}$) for a given wavelength λ is estimated by

$$\tau_{z,\lambda} = \kappa_0 \int_{|z|}^{\infty} \rho_{s,\lambda} dz, \quad (41)$$

where $\kappa_{0,\lambda}$ is the dust opacity for λ . Because the particles with $s > s_\lambda$ do not contribute to the opacity in the Rayleigh regime, the effective dust density for the opacity, $\rho_{s,\lambda}$, is given by

$$\rho_{s,\lambda} \sim \frac{\Sigma_d}{\sqrt{2\pi} H_d} \exp\left(-\frac{z^2}{2H_d^2}\right) \times \left(\frac{s_\lambda}{s_{max}}\right)^{0.5}, \quad (42)$$

where H_d is the scale height of dust particles given by

$$H_d = \sqrt{\frac{\alpha}{\alpha + St(s_\lambda, z)}} H_g, \quad (43)$$

and we used the relation that the mass fraction (ζ) of particles of $s \leq s_\lambda$ is $\sim \sqrt{s_\lambda / s_{max}}$ with the assumed size distribution, $dN(s) \propto s^{-3.5} ds$.¹ In summary, the vertical optical depth is rewritten as

$$\tau_{z,\lambda} = \kappa_0 \Sigma_d \left(\frac{s_\lambda}{s_{max}}\right)^{0.5} \text{erfc}\left(\frac{|z|}{\sqrt{2} H_d}\right). \quad (44)$$

We assumed $\lambda = 0.6 \mu\text{m}$ and $\kappa_0 \sim 2.5 \times 10^4 \text{ cm}^2 \text{ g}^{-1}$, following Binkert & Birnstiel (2023). We also considered the FUV radiation from the central star. Because of the flaring of the disk, the optical depth from the central star is given by $\tau_r = \tau_z / \Phi$, where Φ is the flaring angle set to 0.05 in our calculations. Figure 5 shows the bottom of the FUV-exposed layer ($\tau_r \sim 1$) for the initial condition of each parameter set.

¹ $\zeta = \int_{0.1\mu\text{m}}^{s_\lambda} s^3 (dN/ds) ds / \int_{0.1\mu\text{m}}^{s_{max}} s^3 (dN/ds) ds \simeq (s_\lambda / s_{max})^{0.5}$

2.4.2. Photolysis rate

The photolysis timescale is estimated by the mean collision time of a photon with a carbon atom of amorphous hydrocarbons (Klarmann et al. 2018; Binkert & Birnstiel 2023):

$$t_{\text{ph}} = \frac{4s\rho_c}{3Y_{\text{ph}}F_{\text{FUV}}m_c}, \quad (45)$$

where F_{FUV} is the flux of FUV radiation given by

$$F_{\text{FUV}} = \frac{L_{\text{FUV}}}{4\pi r^2} \exp(-\tau_r). \quad (46)$$

Here, Y_{ph} is the yield of photolysis per incoming photon, and m_c and ρ_c is the atomic mass and the bulk density of carbons. We set the yield $Y_{\text{ph}} = 10^{-4}$. As Binkert & Birnstiel (2023) suggested photons that penetrate the lower layer could destroy more amorphous hydrocarbons because more particles exist in the lower layer. However, this effect could lower the height of photolysis occurring region only by $\lesssim 0.5 H_g$ (see also Fig.3 in Binkert & Birnstiel (2023)).

2.4.3. Oxidation rate

We assume that oxidation occurs only in the exposed layer ($\tau_r \leq 1$), since Lee et al. (2010) showed that oxygen atoms are abundant in the FUV-exposed layer and the abundance decreased steeply with the decrease of the height. We calculate the timescale of oxidation described by

$$t_{\text{ox}} = \frac{4s\rho_c}{3n_{\text{ox}}v_{\text{ox}}Y_{\text{ox}}m_c}, \quad (47)$$

where v_{ox} is the mean thermal velocity of oxygen atoms given by $v_{\text{ox}} = \sqrt{(8/\pi)(k_B T_{\text{FUV}}/m_{\text{ox}})}$, m_{ox} is the oxygen atom mass, and Y_{ox} is the number of carbon atoms removed by an oxygen atom given by (Draine 1979)

$$Y_{\text{ox}} = A \exp\left(-\frac{B}{T_{\text{FUV}}}\right), \quad (48)$$

with $A = 2.3$, $B = 2580 \text{ K}$ for $T_{\text{FUV}} < 440 \text{ K}$ and $A = 170$, $B = 4430 \text{ K}$ for $T_{\text{FUV}} > 440 \text{ K}$. We estimated the number density of oxygen atoms $n_{\text{ox}} = \epsilon n_{\text{H}_2}$, where n_{H_2} is the number density of H_2 given by

$$n_{\text{H}_2} = \frac{\Sigma_g}{\sqrt{2\pi}\mu m_p H_g} \exp\left(-\frac{z^2}{2H_g^2}\right). \quad (49)$$

We assumed $\epsilon = 10^{-4}$, following Klarmann et al. (2018).

3. Results

3.1. Detailed evolution in the fiducial run

In this section, we show the result of the fiducial run with the disk parameters and the fragmentation velocities in Table 2, assuming that all the refractory carbons are amorphous hydrocarbons

Figure 6 shows a typical trajectory in the z - r and s - r planes of a super-particle which starts at $r \approx 9 \text{ au}$ with $s = 0.1 \mu\text{m}$. In the early phase, growth dominates over drift. In this run, the particle is mostly in a viscously heated region, except for the initial stage (Eq. (8)). Substituting the disk temperature given by Eq. (7) into Eq. (32), the fragmentation-limited Stokes number is $\text{St}_{\text{frag}} \approx 0.059 (r/9 \text{ au})^{3/7}$. When the particle's St value exceeds

St_{frag} , we randomly re-assign its size ($< s_{\text{frag}}$) to a weight corresponding to the given power law. The particle grows up to the size corresponding to $\text{St} \sim 0.06$ around 9 au. After the particle passes the snow line at $r_{\text{snow}} \approx 3.7 \text{ au}$, smaller particles are released to be strongly coupled to the gas ($\text{St} < \alpha$) as a result of the evaporation of icy mantle of the pebbles. Finally, the particle is lifted up inside r_{snow} .

Figure 7 shows the snapshots of size and vertical distributions of the particles. The colors of particles show the carbon fraction of each particle. The dark navy dots indicate the silicate super-particles that preserve original carbon fraction similar to the solar value ($f_c \sim 0.25$). The yellow dots inside the snow line represent the silicate super-particles with significantly depleted carbon fraction ($f_c \lesssim 0.01$). The green ones are in between. The size of particles is dramatically changed at the snow line ($\sim 3.7 \text{ au}$) due to the difference in stickiness between icy ($v_{\text{frag}} = 10 \text{ m/s}$) and silicate ($v_{\text{frag}} = 1 \text{ m/s}$) particles, as shown in Eq. (32). The mass averaged size of particles is $\sim s_{\text{max}}/3$, where s_{max} is the maximum dust size (Eq. 31). The particle size is usually limited by fragmentation rather than drift. The upper panel in Fig. 7(a) shows that most of the icy pebbles grow up to the size given by s_{max} (Eq.(31)).

For the icy pebbles, $\text{St} > \alpha$, and their motions are not strongly coupled to the gas, while the motions of the released silicate are strongly coupled ($\text{St} < \alpha$), and the vertical distribution is expanded up to $|z|/r \sim 0.1$. As a result, the aspect ratio of the icy pebble distribution is considerably lower than that of the small silicate particles (the upper panel in Fig. 7(a)), and icy pebbles beyond the snow line are usually shielded from FUV from the host star.

Because the contrasts in v_{frag} and St/α between inside and beyond r_{snow} lead to the significant depletion of solid carbon inside r_{snow} , we explain the growth, drift, and diffusion of particles together with the evolution of f_c in details. The evolution of the radial distribution of the particles is divided into four stages and the carbon fraction is changed according to the stages.

3.1.1. Quasi-steady dust accretion stage

The theoretical estimate for pebble formation timescale due to pairwise coagulation in the Epstein regime is (Sato et al. 2016; Ida et al. 2019)

$$t_{\text{pf}} \sim 2 \times 10^5 \left(\frac{Z_0}{0.01}\right)^{-1} \left(\frac{r}{100 \text{ au}}\right)^{3/2} \text{ years}, \quad (50)$$

where Z_0 is the initial solid-to-gas ratio in the disk. Thus, pebble formation proceeds in an inside-out manner. At $t \sim 0.2 \text{ Myrs}$, the pebbles at $r \lesssim 100 \text{ au}$ have already started drifting and the quasi-steady accretion of solids with the silicate particle pile-up inside the snow line has been established.

Because the mean radial velocity of the silicate particles is lower than that of the icy pebbles, the silicate particles released by sublimation of the icy mantle of the pebbles pile up inside the snow line (see the line at $t = 0.2 \text{ Myr}$ in the top panel of Fig. 8). Since the solid mass flux should be continuous at the snow line, the ratio of solid surface densities from just inside the snow line $\Sigma_{\text{d,in}}$ to just outside $\Sigma_{\text{d,out}}$ is given by

$$\frac{\Sigma_{\text{d,in}}}{\Sigma_{\text{d,out}}} = \frac{0.5\dot{M}_d}{2\pi r v_{r,\text{in}}} \frac{2\pi r v_{r,\text{out}}}{\dot{M}_d} = 0.5 \frac{v_{r,\text{out}}}{v_{r,\text{in}}}, \quad (51)$$

where we assume half of the solid mass is converted to the water vapor inside the snow line. Equation (20) is rewritten as

$$v_r \approx -\frac{\Lambda}{1 + \Lambda^2 \text{St}^2} \left(2\Lambda \text{St} C_\eta + \frac{3}{2}\alpha\right) h_g^2 r \Omega. \quad (52)$$

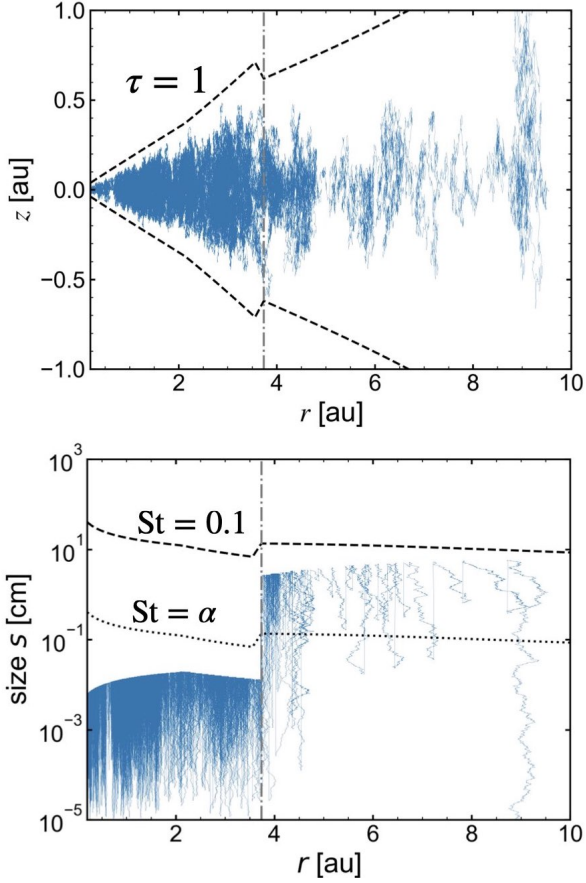


Fig. 6: Typical trajectory of a solid particle (upper panel) and the size evolution (lower panel) in a disk with the fiducial parameters. The gray dash-dotted line represents the snow line at $r_{\text{snow}} \approx 3.7$ au. The black dotted line of the top panel shows the height of the FUV-exposed layer. The black dotted and dashed lines show the particle sizes corresponding to $St = 0.1$ and $St = \alpha$, respectively.

Inside the snow line, since the released silicate particles are small enough to be coupled with the gas ($St \ll \alpha$), their radial velocity is

$$v_{r,\text{in}} \approx -\frac{3\Lambda}{2}\alpha h_g^2 r \Omega. \quad (53)$$

Outside the snow line, $St \gg \alpha$ for icy pebbles and the radial drift velocity is given by

$$v_{r,\text{out}} \approx -2\Lambda^2 St C_\eta h_g^2 r \Omega. \quad (54)$$

With $\Lambda \approx 1$, we obtain

$$\frac{\Sigma_{d,\text{in}}}{\Sigma_{d,\text{out}}} \approx 0.5 \times \frac{4C_\eta St_{\text{frag}}}{3 \times 3 \alpha} \approx 6 \left(\frac{\alpha}{10^{-3}} \right)^{-2} \left(\frac{v_{\text{frag,ice}}}{10 \text{ m/s}} \right)^2 \left(\frac{T(r_{\text{snow}})}{170 \text{ K}} \right)^{-1}, \quad (55)$$

where we substitute Eq. (32) into $St \sim St_{\text{frag}}/3$ (taking the size distribution into account) and use $C_\eta = 11/8$. The numerical result at $t = 0.2$ Myr in the top panel of Fig. 8 shows that the jump in Σ_d is consistent with the Eq. (55).

The released silicate particles are occasionally stirred up highly by the disk gas turbulence because $St \ll \alpha$, while they radially go back and forth. As a result, some fraction of amorphous hydrocarbons in these particles are destructed by photolysis and oxidation.

However, f_c decreases only slightly at $t = 0.2$ Myrs (Fig. 8(b)) because fresh silicate particles full of amorphous hydrocarbons are steadily supplied and well mixed with particles where the amorphous hydrocarbons become destructed. This is consistent with the result found by Klarmann et al. (2018).

To highlight the effect of the continuous supply, we carried out a hypothetical case where all the radial motion is set to zero. Because the pebble flux is also stopped, the fresh refractory carbon supply is also stopped. The carbon fraction changes only through vertical diffusion, photolysis, and oxidation. As shown by the black line in Fig. 9, this process efficiently depletes f_c on a timescale of 50 kyrs.

3.1.2. Icy pebble flux decaying stage

However, the quasi-steady accretion ends, and the carbon depletion pattern changes, when the pebble formation front reaches the disk's outer edge at the characteristic radius r_{disk} . Then, because most of the reservoir of solid materials is consumed, the pebble flux rapidly decays (Sato et al. 2016; Ida et al. 2019).

The duration of the quasi-steady supply of icy pebbles is given by $t_{\text{pf}}(r_{\text{disk}}) + t_{\text{drift,ice}}$, where $t_{\text{drift,ice}}$ is the drift timescale from the disk outer edge to the snow line. The drift velocity is given by

$$\begin{aligned} v_r &\approx 2\Lambda^2 St C_\eta h_g^2 r \Omega \\ &\approx 7.8 \times 10^{-5} \Lambda^2 \left(\frac{\alpha}{10^{-3}} \right)^{-1} \left(\frac{v_{\text{frag}}}{10 \text{ m/s}} \right)^2 \left(\frac{r}{1 \text{ au}} \right)^{1/2} \text{ au/y}, \end{aligned} \quad (56)$$

Because $h_g^2 \propto T$, the T -dependence is canceled out with T^{-1} in $St \approx St_{\text{frag}}/3$. The α -dependence appears from $St \propto 1/\alpha$ in the fragmentation limit. The factor $\Lambda = (1 + \rho_d/\rho_g)^{-1}$ is estimated by

$$\begin{aligned} \frac{\rho_d}{\rho_g} &= \frac{\Sigma_d H_g}{\Sigma_g H_d} \sim \frac{\Sigma_d}{\Sigma_g} \sqrt{\frac{St}{\alpha}} \\ &\approx 0.13 \left(\frac{\Sigma_d/\Sigma_g}{0.01} \right) \left(\frac{\alpha}{10^{-3}} \right)^{-1} \left(\frac{v_{\text{frag}}}{10 \text{ m/s}} \right) \left(\frac{r}{100 \text{ au}} \right)^{3/14}. \end{aligned} \quad (57)$$

Here, we use Eq. (43) for H_d assuming $St \gg \alpha$ and the irradiation-dominated T distribution is applied in the regions outside the snow line (Eq. (7)). Then, $t_{\text{drift,ice}}$ is estimated as

$$\begin{aligned} t_{\text{drift,ice}} &= - \int_{r_{\text{snow}}}^{r_{\text{disk}}} \frac{dr}{v_r} \sim 3.1 \times 10^5 \left(\frac{\alpha}{10^{-3}} \right) \left(\frac{10 \text{ m/s}}{v_{\text{frag,ice}}} \right)^2 \\ &\times \left(\frac{1 + \rho_d/\rho_g}{1.1} \right)^2 \left(\sqrt{\frac{r_{\text{disk}}}{100 \text{ au}}} - 0.1 \sqrt{\frac{r_{\text{snow}}}{1 \text{ au}}} \right) \text{ years}. \end{aligned} \quad (59)$$

In the fiducial run, $t_{\text{drift,ice}}$ is estimated to be about 2.5×10^5 years.

The second stage starts at $t \sim t_{\text{pf}} + t_{\text{drift,ice}}$ (~ 0.45 Myr in the fiducial run). In this stage, while Σ_d inside the snow line has not been reduced, the carbon fraction f_c starts decreasing. Figure 7(b) shows the vertical and size distributions at $t = 0.45$ Myr. The total mass of dust particles inside r_{snow} is larger than that outside it, since most of the icy pebbles carrying silicate particles had drifted to the regions inside r_{snow} . The upper panel of Fig. 8 shows the evolution of Σ_d . The Σ_d beyond r_{snow} significantly drops from the first phase ($t = 0.2$ Myr) to the second phase ($t = 0.45$ Myr), while the Σ_d decay is not significant inside r_{snow} . As a result, Σ_d jumps at r_{snow} by as much as a factor of 30. However, carbon depletion proceeds only by a factor of a few from the first to the second stage, because supply of icy pebbles still remains at a reduced rate.

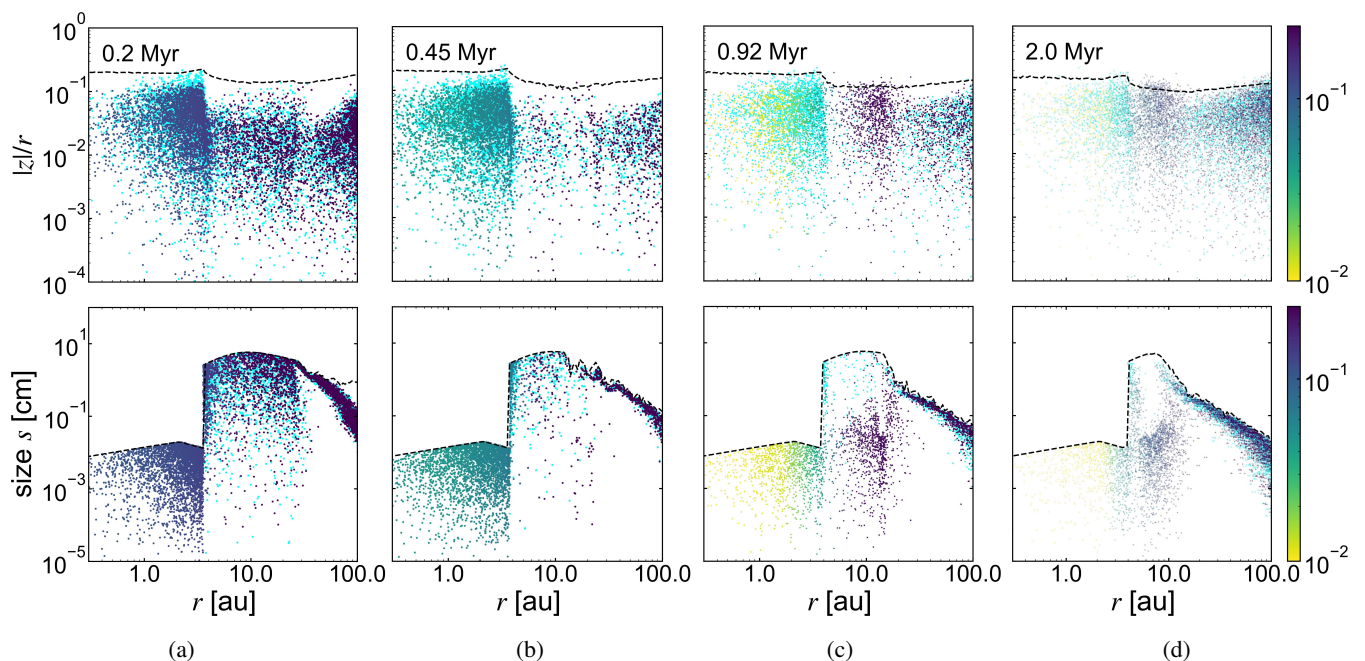


Fig. 7: Snapshots of solid super-particles in the r - $(|z|/r)$ plane and size distribution. The upper panels show the snapshots of silicates at (a) 0.2 Myrs ($\sim t_{\text{pf}}$), (b) 0.45 Myrs ($\sim t_{\text{pf}} + t_{\text{drift,ice}}$), (c) 0.92 Myrs ($\sim t_{\text{pf}} + t_{\text{drift,ice}} + t_{\text{diff,snow}}$), and (d) 2.0 Myrs. The color bar shows the carbon fraction of each silicate super-particle. The cyan dots show the icy super-particles. The black dashed line shows the height of $\tau_{\text{FUV}} = 1$. The lower panels show the size distributions of silicates corresponding to the upper panels. The black dashed line shows the local maximum dust size (s_{max}) (Eq. 31).

3.1.3. Silicate dust surface density decaying stage

In the third stage, Σ_{d} decreases also inside r_{snow} . Because the influx of silicate particles from the outer region is already diminished, the decrease occurs on a diffusion timescale at r_{snow} (Okamoto & Ida 2022):

$$t_{\text{diff,snow}} \sim \frac{r^2}{\alpha H_{\text{g}}^2 \Omega_{\text{K}}} \Big|_{r_{\text{snow}}} = \frac{1}{\alpha h_{\text{g}}^2 \Omega_{\text{K}}} \Big|_{r_{\text{snow}}} \\ \sim 4.7 \times 10^5 \left(\frac{\alpha}{10^{-3}} \right)^{-10/9} \left(\frac{\dot{M}_{\text{g}}}{10^{-8} M_{\odot} \text{ yr}^{-1}} \right)^{2/9} \text{ years.} \quad (60)$$

In the fiducial run, $t \sim t_{\text{pf}} + t_{\text{drift,ice}} + t_{\text{diff,snow}} \sim 0.92$ Myrs. The upper panel of Fig. 8 shows that at $t = 0.92$ Myrs, Σ_{d} inside r_{snow} is decreased by a factor of several from that at $t = 0.45$ Myr.

In this stage, f_{c} shows a pronounced hyperbolic-tangent-function-like (tanh-like) depletion pattern near the snow line by more than one order of magnitude (the line of $t = 0.92$ Myr). The greater depletion is due to the diminished influx of silicate particles from the outer region. The flat f_{c} pattern at ≤ 1 au is caused by higher Σ_{d} there. Because photolysis is inefficient there, f_{c} conserves that in the outer region.

The pronounced decrease in f_{c} around r_{snow} is not originated mainly by the shadow effect, that amorphous hydrocarbons are not destroyed outside r_{snow} due to the FUV shielding that we adopt (Sect. 2.2.2). In Fig. 10, the fiducial case result is compared with the result without the shadow effect at 0.68 Myrs ($\sim t_{\text{pf}} + t_{\text{drift,ice}} + 0.5t_{\text{diff,snow}}$), where the similar drop-off in f_{c} around r_{snow} is shown. While f_{c} is decreased at $r \gtrsim r_{\text{snow}}$, the non-shadow effect just lowers the baseline of f_{c} in the inner region.

We have argued that the tanh-like f_{c} pattern is formed by a jump in Σ_{d} across r_{snow} . After 0.92 Myr, since Σ_{d} is depleted also inside r_{snow} , it could be predicted that f_{c} goes up again. However, Fig. 8 shows that f_{c} further decreases while the enhanced

jump in Σ_{d} at $\sim r_{\text{snow}}$ disappears. This is caused by more efficient photolysis, associated with the opacity decrease due to the Σ_{d} decay, which overwhelms the effect of the reduced jump of Σ_{d} at $\sim r_{\text{snow}}$. As this effect also narrows the area where f_{c} is flat, the tanh-like f_{c} pattern is diminished.

3.2. Analytical formula for Σ_{d} across the snow line

We found that the carbon fraction inside the snow line is regulated by the ratio of Σ_{d} inside and outside the snow line, except for the final phase with highly depleted Σ_{d} . To explain the numerical results, we analytically estimate the Σ_{d} distribution.

The solid-to-gas ratio with $\Lambda \ll 1$ is given by (Eq. (53)):

$$Z = \frac{\Sigma_{\text{d}}}{\Sigma_{\text{g}}} = \frac{2\pi r |u_{\text{v}}| \dot{M}_{\text{d}}}{2\pi r |v_{\text{r}}| \dot{M}_{\text{g}}} \simeq \frac{3\alpha h_{\text{g}}^2 / 2}{h_{\text{g}}^2 (2C_{\eta} \text{St} + 3\alpha/2)} \frac{\dot{M}_{\text{d}}}{\dot{M}_{\text{g}}}, \quad (61)$$

In a steady accretion disk region, $\dot{M}_{\text{d}}/\dot{M}_{\text{g}}$ is constant with r . When $\text{St} \ll \alpha$, corresponding to the region at $r < r_{\text{snow}}$,

$$Z \simeq \dot{M}_{\text{d}}/\dot{M}_{\text{g}}. \quad (62)$$

On the other hand, for $\text{St} \gg \alpha$ at $r > r_{\text{snow}}$, $Z \propto \text{St}^{-1}$. As Eqs. (32) and (33) show, the drift limit is more stringent at relatively large r , where the dust density is lower and collisions are less frequent. For $r > r_{\text{dri-fra}}$ (the transition radius between the drift and fragmentation limits), $\text{St} \sim \text{St}_{\text{drift}}/3 \propto Z T^{-1} r^{-1}$ (Eq. (33)). Deleting St from this relation and $Z \propto \text{St}^{-1}$, we obtain

$$Z(r) \simeq Z(r_{\text{disk}}) \left(\frac{T(r)}{T(r_{\text{disk}})} \right)^{1/2} \left(\frac{r}{r_{\text{disk}}} \right)^{1/2}, \quad (63)$$

where r_{disk} is the disk radius. In the outer disk region ($r > r_{\text{vis-irr}}$), irradiation is dominant and $T \propto r^{-3/7}$. Thus,

$$Z = \frac{\Sigma_{\text{d}}}{\Sigma_{\text{g}}} \simeq Z(r_{\text{disk}}) \cdot \left(\frac{r}{r_{\text{disk}}} \right)^{2/7}. \quad (64)$$

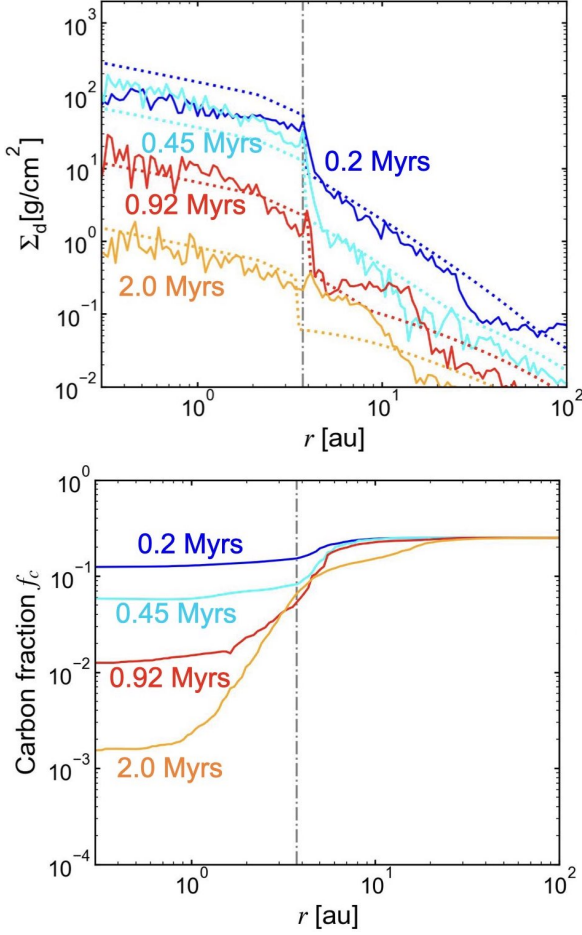


Fig. 8: Time evolution of the solid surface density Σ_d (upper panel) and the carbon fraction, f_c , (lower panel) of the fiducial run. The gray dash-dotted line shows the snow line. The dotted lines in the upper panel show the analytical estimations given by Eq. (68). The dash-dotted lines represent the snow line at $r_{\text{snow}} \sim 3.7$ au.

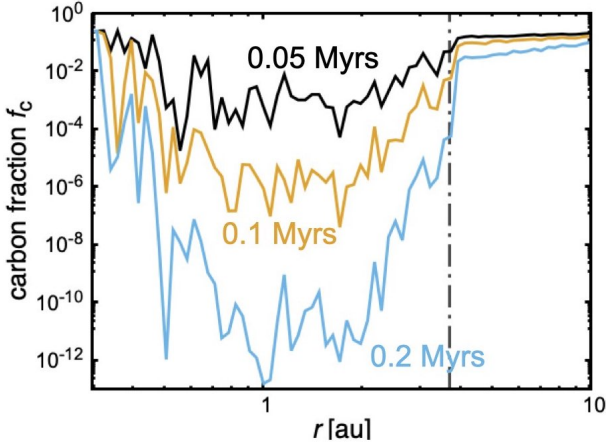


Fig. 9: Time evolution of carbon fraction, f_c , when the particles diffuse only vertically and neither drift nor diffuse radially.

Substituting this equation into Eq. (33), we obtain

$$\text{St}_{\text{drift}} = 0.13 \left(\frac{Z(r_{\text{disk}})}{10^{-3}} \right) \left(\frac{r}{1 \text{ au}} \right)^{-5/7} \left(\frac{r_{\text{disk}}}{100 \text{ au}} \right)^{-2/7} \left(\frac{T}{150 \text{ K}} \right)^{-1}. \quad (65)$$

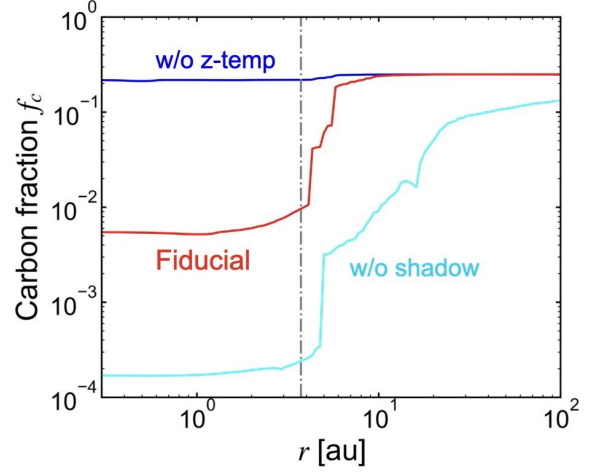


Fig. 10: Carbon fraction, f_c , at 0.68 Myr in the fiducial run, without the vertical temperature profile, and without the shadow area outside the snow line.

Comparing this with Eq. (32), the transition radius $r_{\text{dri-fra}}$ is given by

$$r_{\text{dri-fra}} = 11 \left(\frac{Z(r_{\text{disk}})}{10^{-3}} \right)^{7/5} \left(\frac{r_{\text{disk}}}{100 \text{ au}} \right)^{-2/5} \left(\frac{v_{\text{frag}}}{10 \text{ m/s}} \right)^{-14/5} \left(\frac{\alpha}{10^{-3}} \right)^{7/5} \text{ au}. \quad (66)$$

For $r < r_{\text{dri-fra}}$, $Z \propto \text{St}^{-1}$ with Eq. (32) shows

$$Z(r) \simeq Z(r_{\text{dri-fra}}) \left(\frac{T(r)}{T(r_{\text{dri-fra}})} \right). \quad (67)$$

Inside the snow line, Z is constant with r (Eq. (62)). Because $\Sigma_g \propto r^{-1/2}$ in this region (Eqs. (1) and (6)), $\Sigma_d \propto r^{-1/2}$. The ratio of Σ_d just inside the snow line to just outside it is given by Eq. (55). Thus, in the steady accretion disk regions,

$$Z(r) = \begin{cases} Z(r_{\text{disk}}) \left(\frac{r}{r_{\text{disk}}} \right)^{2/7} & [r > r_{\text{dri-fra}}] \\ Z(r_{\text{dri-fra}}) \left(\frac{T(r)}{T(r_{\text{dri-fra}})} \right) & [r_{\text{snow}} < r < r_{\text{dri-fra}}] \\ Z(r_{\text{snow}}) \times 6 \left(\frac{\alpha}{10^{-3}} \right)^{-2} \left(\frac{v_{\text{frag,ice}}}{10 \text{ m/s}} \right)^2 & \\ \times \left(\frac{T(r_{\text{snow}})}{170 \text{ K}} \right)^{-1} \left(\frac{r}{r_{\text{snow}}} \right)^{-1/2} & [r < r_{\text{snow}}]. \end{cases} \quad (68)$$

Here, $Z(r_{\text{dri-fra}}) = Z(r_{\text{disk}})(r_{\text{dri-fra}}/r_{\text{disk}})^{2/7}$ and $Z(r_{\text{snow}}) = Z(r_{\text{dri-fra}})(T(r_{\text{snow}})/T(r_{\text{dri-fra}}))$. The steady accretion across the snow line would continue until Σ_d inside the snow line starts to decay ($t \sim t_{\text{pf}} + t_{\text{drift,snow}} \sim 0.45$ Myrs).

Equation (68) shows that once $Z(r_{\text{disk}})$ is given, the Σ_d distribution is estimated ($\Sigma_d = Z \Sigma_g$; Σ_g is given by the simulation parameter \dot{M}_g). Before the pebble formation front arrives at r_{disk} , $Z(r_{\text{disk}})$ is given by its initial value $Z_0 \sim 0.01$. After that, $Z(r_{\text{disk}})$ is rapidly reduced. Ida et al. (2019) derived the time evolution of $Z(r_{\text{disk}})$ as

$$Z(r_{\text{disk}}) \sim Z_0 (1 + t/t_{\text{pf}})^{-\gamma}, \quad (69)$$

where

$$\gamma \sim 1 + 0.15 (300 \text{ au}/r_{\text{disk}}). \quad (70)$$

The dashed lines in the upper panel of Fig. 8 show the analytical estimate of Σ_d given by substituting Eq. (69) into Eq. (68). The Σ_d distribution at $\geq r_{\text{snow}}$ is well fitted by the analytical estimate for all of the four different times (0.2–1.5 Myr). At $t = 0.45$ and 0.92 Myrs, it is fitted also in the region inside the snow line except for the innermost region. For this duration, Σ_d is also decaying and the steady accretion is established.

3.3. Important parameters for carbon depletion

3.3.1. The v_{frag} change across the snow line

Detailed descriptions of the evolution of particles in Sect. 3.1 strongly suggest that the conditions for the tanh-like pattern of f_c are an enhanced jump in Σ_d at $\sim r_{\text{snow}}$ and early decay of icy pebble flux that reduces the supply of fresh amorphous hydrocarbons to the region inside r_{snow} . The both features are originated from $v_{\text{frag,sil}} < v_{\text{frag,ice}}$ such that $\text{St} \sim \alpha$ at $r < r_{\text{snow}}$ and $\text{St} \gg \alpha$ at $r > r_{\text{snow}}$.

The decay of icy pebble flux starts at $t \sim t_{\text{pf}} + t_{\text{drift,ice}}$ where t_{pf} and $t_{\text{drift,ice}}$ are given by Eqs. (50) and (59). For $Z_0 = 0.01$ and $r_{\text{snow}} = 3.7$ au, we have

$$t_{\text{pf}} \sim 2 \times 10^5 \left(\frac{r_{\text{disk}}}{100 \text{ au}} \right)^{3/2} \text{ years}, \quad (71)$$

$$t_{\text{drift,ice}} \sim 2.5 \times 10^5 \left(\frac{\alpha}{10^{-3}} \right) \left(\frac{10 \text{ m/s}}{v_{\text{frag,ice}}} \right)^{-2} \left(\frac{r_{\text{disk}}}{100 \text{ au}} \right)^{1/2} \text{ years}. \quad (72)$$

The drift timescale is shorter for larger $v_{\text{frag,ice}}$. For the early decay of the supply of fresh amorphous hydrocarbons to occur, $t_{\text{drift,ice}}$ must be short enough compared with global disk gas depletion timescale $t_{\text{disk}} \sim 3 \times 10^6 (\alpha/10^{-3})^{-1} (r_{\text{disk}}/100 \text{ au})$ yrs, which is equivalent to

$$v_{\text{frag,ice}} \gtrsim 3.2 \left(\frac{\alpha}{10^{-3}} \right) \left(\frac{r_{\text{disk}}}{100 \text{ au}} \right)^{-1/4} \text{ m/s}. \quad (73)$$

Here, we confirm the above conditions by performing the runs with different combinations of $v_{\text{frag,ice}}$ and $v_{\text{frag,sil}}$. Figure 11 shows Σ_d and f_c at 0.68 Myr for $v_{\text{frag,ice}} = v_{\text{frag,sil}} = 10$ m/s (the blue line), $v_{\text{frag,ice}} = v_{\text{frag,sil}} = 1$ m/s (the cyan line), and the fiducial case (the red line) at 0.68 Myr, which is the intermediate time of the third stage ($\sim t_{\text{pf}} + t_{\text{drift,ice}} + 0.5t_{\text{diff,snow}}$). To highlight the v_{frag} effect, the shadow effect is applied even in the case of $v_{\text{frag,ice}} = v_{\text{frag,sil}}$. The results without the shadow effect are shown in Appendix B.

In the run with $v_{\text{frag,ice}} = v_{\text{frag,sil}} = 1$ m/s, for both silicate particles and ice pebbles, $\text{St} = 2.1 \times 10^{-4}$ at the snow line. Because $\text{St} < \alpha$, silicate particles do not accumulate inside the snow line and f_c decreases only slightly inside r_{snow} .

When $v_{\text{frag,ice}} = v_{\text{frag,sil}} = 10$ m/s, for both silicate particles and ice pebbles, $\text{St} = 2.1 \times 10^{-2}$ at the snow line, and particles are also not piled up except around the snow line. Since the pile-up around the snow line is caused by recondensation of water vapor diffusing out from inside the snow line, it does not significantly influence the motions of the silicate particles, and f_c decreases only slightly as well.

On the other hand, when $v_{\text{frag,ice}} = 10$ m/s and $v_{\text{frag,sil}} = 1$ m/s, $\text{St} = 2.1 \times 10^{-4} < \alpha$ for silicate particles and $\text{St} = 2.1 \times 10^{-2} > \alpha$. Accordingly, the pile-up occurs and f_c significantly decreases with the tanh-like shape.

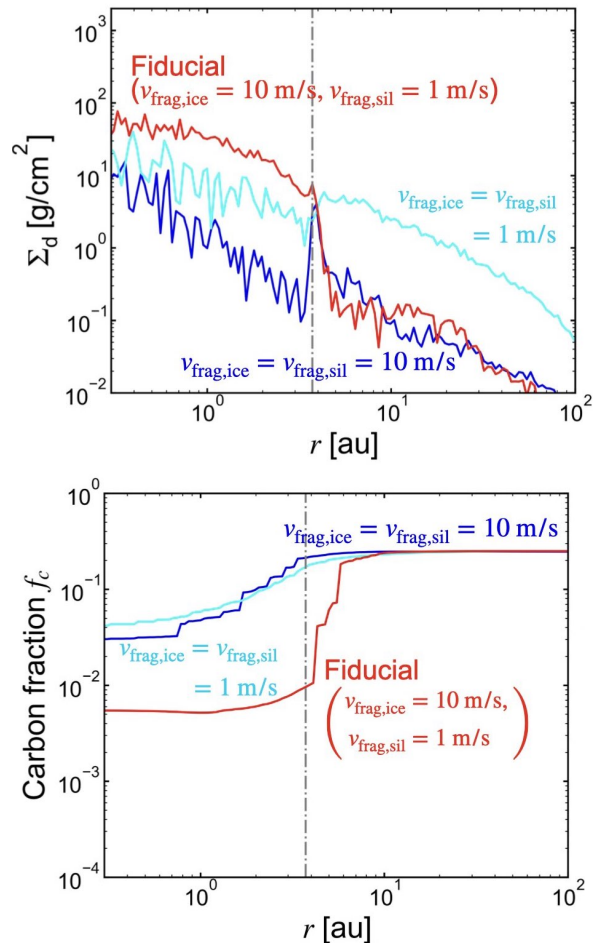


Fig. 11: Distributions of Σ_d and f_c at 0.68 Myrs for $v_{\text{frag,ice}} = v_{\text{frag,sil}} = 1$ m/s and 10 m/s and the fiducial case ($v_{\text{frag,ice}} = 10$ m/s and $v_{\text{frag,sil}} = 1$ m/s).

3.3.2. The vertical temperature profile

The upper panel of Fig. 12 shows f_c at 0.1 Myr with and without vertical temperature profile (see Fig. 3). To highlight this effect, we stop the radial motion of particles. The carbon fraction f_c is the minimum at $r \sim 1 - 2$ au. The lower panel shows the ratio of vertical diffusion timescale in the FUV-exposed layer to that at the mid-plane. The ratio is the smallest at $r \sim 2$ au inside r_{snow} . Because the temperature is significantly higher in the upper layer than around the mid-plane at ~ 1 au, the diffusion there leads to more photodegradation of amorphous hydrocarbons. The carbon fraction outside the snow line (~ 3.7 au) does not decrease because the icy pebbles are not particularly stirred up. While the radial drift is neglected in Fig. 12, a significant impact of the vertical temperature profile on the carbon depletion is also shown in Fig. 10, where the radial drift is included.

3.3.3. Other parameter dependencies

We also carried out runs with a different value for each parameter from the fiducial run, $\alpha = 5 \times 10^{-4}$, $v_{\text{frag,sil}} = 0.1$ m/s, and $Z_0 = 0.05$. In these cases, $\text{St} \lesssim \alpha$ inside r_{snow} and $\text{St} \gg \alpha$ outside it, which is equivalent to the two conditions of the pile-up of silicate particles and earlier decay of icy pebble flux are satisfied. In these cases, the tanh-like shaped f_c pattern is produced with small variations in the bottom values (Fig. 13), as expected. The detail results are shown in Appendix C.

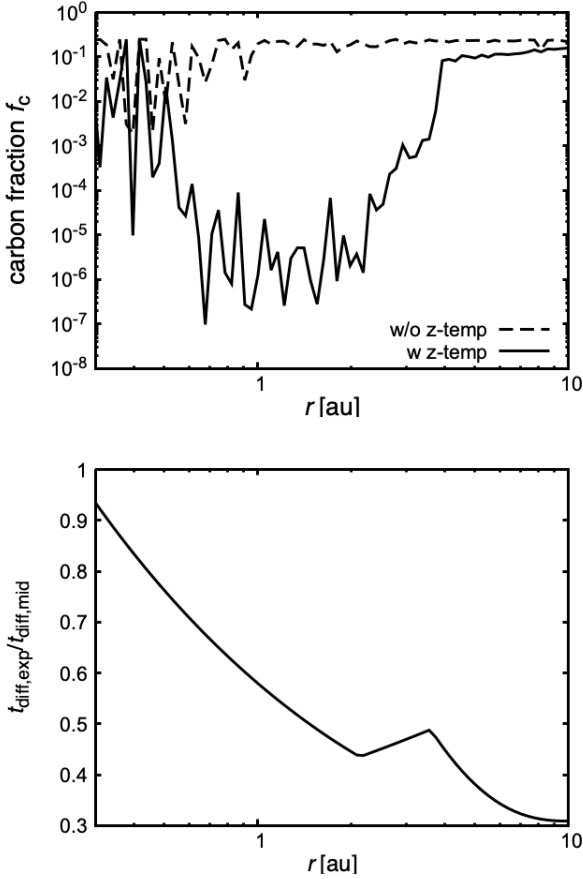


Fig. 12: Carbon fraction at 0.1 Myr with and without vertical temperature profile (upper panel) and ratio of vertical diffusion timescale at FUV-exposed layer to mid-plane (lower panel). In these runs, the radial drift is neglected to highlight the effect of the vertical temperature profile.

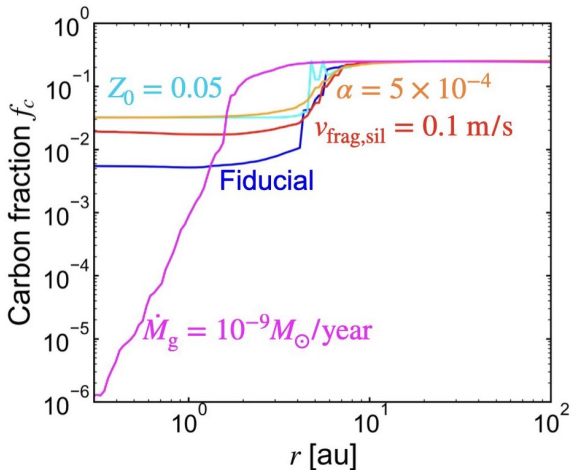


Fig. 13: Carbon fraction at 0.68 Myrs for different parameter sets.

The only exception is the case with $\dot{M}_g = 10^{-9} M_\odot/\text{yr}$, where the disk opacity is significantly lower. As the silicate particles drift to inner regions, the carbon destruction proceeds to result in qualitatively different f_c shape.

4. Discussion

4.1. Pyrolysis of complex organics

So far we have not included complex organics, because it is likely that some fraction of the products of their pyrolysis are amorphous hydrocarbons (Sect. 1). In Fig. 14, we show the result with initial solid carbon of a mixture of complex organics with $T_{\text{des}} = 540\text{K}$ (50 wt.%) and amorphous hydrocarbons (50 wt.%). The simulation parameters are the same as the fiducial case. The pyrolysis of complex organics occurs even near the disk mid-plane. In the runs in Fig. 14, however, we still assume that half the mass of the complex organics is converted into amorphous hydrocarbons through this reaction. Even though at 0.92 Myr, the total carbon fraction f_c inside the pyrolysis line shows a slightly lower value than outside of it, the difference is not significant enough to explain the discrepancy between chondrites and the bulk Earth.

The initial ratio of complex organics and amorphous hydrocarbons and the conversion rate of complex organics to amorphous hydrocarbons through pyrolysis remain unclear. Adjusting these values could allow the f_c pattern to better reproduce the lower f_c observed in the bulk Earth compared to chondrites.

4.2. FUV radiation outside the snow line

We assumed carbon destruction does not occur outside the snow line because FUV radiation from the host star is hindered by piled-up dust inside the snow line. However, the ‘‘shadow area’’ may only extend up to ~ 10 au (Ohno & Ueda 2021).

However, this could not be effective enough to erase the dichotomy in f_c between the inner and outer disk regions. As shown in Fig. 10, the f_c distribution shows the tanh-like pattern also in the case without the shadow area. This result suggests that the limited shadow region and the interstellar FUV radiation do not break the higher carbon fraction at the outer disk region than the inner disk region. However, as discussed in Sect 4.5, the result without the shadow area may be inconsistent with the observation of the comets.

4.3. Oxidation

We assumed amorphous hydrocarbon is oxidized only if the dust exists in the FUV-exposed layer ($\tau \lesssim 1$). However, a few oxygen atoms might exist in the lower layer (e.g., Lee et al. 2010; Anderson et al. 2017). Therefore, oxidation in the lower layer might reduce the carbon abundance.

Moreover, the carbon particle might be oxidized by OH radicals (e.g., Finocchi et al. 1997; Gail & Tieloff 2017). OH radicals are thought to be formed by thermal dissociation of H_2O at the hotter region ($T \gtrsim 1100\text{K}$) (e.g., Gail & Tieloff 2017). The abundance of OH radicals in the inner disk region has some uncertainty as Finocchi et al. (1997) estimated $10^{-10} - 10^{-7}$ relative to H_2 and Gail & Tieloff (2017) calculated $10^{-12} - 10^{-9}$ relative to H_2 at $T \gtrsim 1100\text{K}$. Although the OH abundance is not expected to be high, oxidation by OH might also reduce more carbon particles (Gail & Tieloff 2017). The calculation with a more accurate estimation of OH radical and oxygen atom abundances is left to a future study.

4.4. Other processes: Gap or pressure bump in the gas disk

Klarmann et al. (2018) concluded that carbon depletion needs some mechanisms that stop the inward solid particles’ flux, such

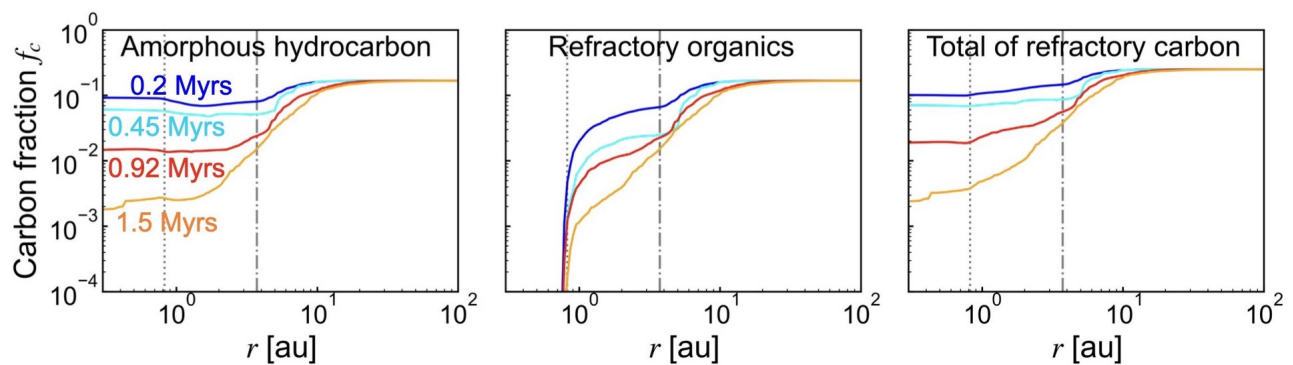


Fig. 14: Carbon fraction, f_c , with a mixture of complex organics with $T_{\text{des}} = 540$ K (50 wt.%) and amorphous hydrocarbons (50 wt.%). The left figure shows the mass fraction of amorphous hydrocarbons, the middle panel shows that of complex organics, and the right panel shows the total carbon fraction. The gray dash-dotted and dotted lines show the snow and pyrolysis lines.

as a gap or a pressure bump in the gas disk. However, the significant reduction in the inward solid particles' flux by the gap or pressure bump should lower Σ_d and the disk optical depth, the flat f_c pattern would not appear (Fig. 13).

Klarmann et al. (2018) calculated the evolution of Σ_d with single-sized particles. The different sizes between icy pebbles and silicate particles released at the snow line cause pile-up of the silicate particles without the gap or pressure bump (Saito & Sirono 2011; Ida & Guillot 2016; Schoonenberg & Ormel 2017; Ida et al. 2021). In this paper, we have shown that this effect can result in significant carbon depletion.

4.5. Comparison to the observational data

It is shown that chondrite meteorites in the matrix scaling universally show $f_c \sim 0.01$ (Fig. 1 and Alexander et al. (2007)). Our simulations show a flat bottom value of the tanh-like shape as $f_c \sim 0.02$ – 0.03 inside the snow line, which is consistent with the chondrite data, if their parent bodies were formed inside the snow line (Fig. 15). The further smaller f_c of the bulk Earth could be potentially accounted for by including complex organics as well as amorphous hydrocarbons and some adjustments of their initial abundance ratio and conversion rate from complex organics to amorphous hydrocarbons through pyrolysis (Sect. 4.1). Comets have f_c as high as ISM, which is also consistent with the tanh-like pattern that our calculations produce (see also Sect. 4.2).

As discussed in Sect. 1, the observed f_c on the WD photospheres, which should reflect the bulk compositions of asteroids or rocky planets around the WDs, is distributed from the solar value far down to the bulk Earth value. We found that the conditions to produce the tanh-like depletion pattern of solid carbon are not too severe, but may be sensitive to details of dust particle properties (and possibly to the disk parameters). This may produce a diversity of f_c values in a range of a few orders of magnitude. It could be responsible for the observed large variety of C/Si ratios on the WD photo-spheres. More detailed comparisons are left for future works.

5. Conclusion

Rocky bodies in the inner Solar System are depleted in carbon compared to the Sun, by one to several orders of magnitude, although most solid carbonaceous components should be refractory in the ISM and the comets. Possible mechanisms to destruct refractory carbonaceous components are photolysis (Alata et al.

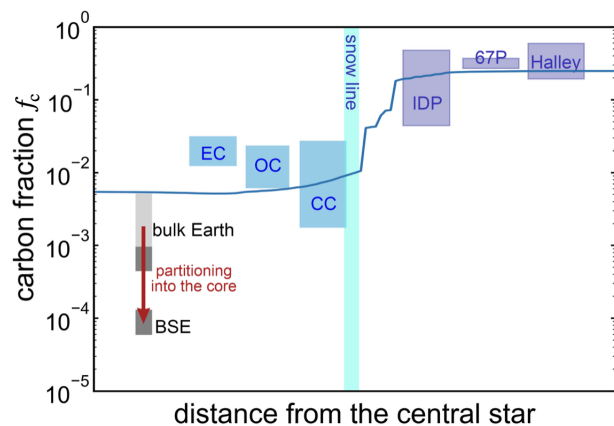


Fig. 15: Expect the formation region for each rocky body based on our calculation results.

2014, 2015) and oxidation for highly refractory carbons such as amorphous hydrocarbons (e.g., Draine 1979) in the upper FUV-exposed layer and pyrolysis for modestly complex organics (e.g., Chyba et al. 1990). However, previous theoretical models (Klarmann et al. 2018; Binkert & Birnstiel 2023) did not succeed in reproducing the observed significant carbon depletion in the case of highly refractory carbons.

We performed a 3D Monte Carlo simulation to track super-particles trajectories in a steady accretion gas disk, taking account of the effects that were not considered in the previous models. We found that the carbon fraction, f_c , is lower by two orders of magnitude inside the snow line when the following conditions are present.

1. The fragmentation limit velocity of silicate particles is lower than that of icy pebbles so that $St \lesssim \alpha$ for silicate particles and $St \gg \alpha$ for icy pebbles.
2. The gas temperature is considerably higher in the upper optically thin layer than near the mid-plane.

The first condition leads to a pile-up of silicate particles inside the snow line and earlier decay of icy pebble flux incoming to the snow line than the depletion of the silicate particles. The latter is shown by globally calculating the growth and radial drift of pebbles in the disk. The second condition leads to more effective vertical diffusion in the upper optically thin layer. Because the FUV-exposed layer is as high as $\sim 4 H_g$, the effective vertical diffusion can significantly enhance photolysis.

The matrix-scaled f_c is similar (one to two orders of magnitude depletion) among carbonaceous, ordinary, and enstatite

chondrites, while the orbital radii of their parent bodies may be diverse. This feature is well reproduced by our simulations with highly refractory carbon (amorphous hydrocarbons). The bulk Earth could have further lower f_c (three to four orders of magnitude depletion). This feature might also be reproduced if the refractory carbon source is a mixture of amorphous hydrocarbons and (modestly) complex organics.

The first and second conditions are not too severe, but still sensitive and their effects could be responsible for the observed large variety of C/Si on white dwarf photo-spheres, which would be polluted by rocky bodies that existed around the white dwarfs. Theoretical investigations of the carbon depletion problem in the inner Solar System can offer insights into the origin of the large variety of C/Si in rocky bodies in exoplanetary systems. If the f_c values of Earth-size planets in exoplanetary habitable zones have a variation by a few (or more) orders of magnitude, the surface environments (and even interiors) of these planets should exhibit a broad scope of diversity. More studies are needed to explore these issues in depth.

Acknowledgements. We thank the referee for his insightful and encouraging comments. We also thank Shogo Tachibana, Hideko Nomura, and Chris Ormel for helpful discussions. This work was supported by JST Tokyo-Tech SPRING, Grant Number JPMJSP2106, and JSPS Kakenhi 23KJ0885 and 21H04512.

References

- Alata, I., Cruz-Diaz, G. A., Muñoz Caro, G. M., & Dartois, E. 2014, *A&A*, 569, A119
- Alata, I., Jallat, A., Gavilan, L., et al. 2015, *A&A*, 584, A123
- Alexander, C. M. O. D., Fogel, M., Yabuta, H., & Cody, G. D. 2007, *Geochim. Cosmochim. Acta*, 71, 4380
- Anderson, D. E., Bergin, E. A., Blake, G. A., et al. 2017, *ApJ*, 845, 13
- Aumatell, G. & Wurm, G. 2011, *MNRAS*, 418, L1
- Bardyn, A., Baklouti, D., Cottin, H., et al. 2017, *MNRAS*, 469, S712
- Bauer, I., Finocchi, F., Duschl, W. J., Gail, H. P., & Schloeder, J. P. 1997, *A&A*, 317, 273
- Bell, K. R. & Lin, D. N. C. 1994, *ApJ*, 427, 987
- Bergin, E. A., Blake, G. A., Ciesla, F., Hirschmann, M. M., & Li, J. 2015, *Proceedings of the National Academy of Science*, 112, 8965
- Binkert, F. & Birnstiel, T. 2023, *MNRAS*, 520, 2055
- Birnstiel, T., Klahr, H., & Ercolano, B. 2012, *A&A*, 539, A148
- Bischoff, D., Kreuzig, C., Haack, D., Gundlach, B., & Blum, J. 2020, *MNRAS*, 497, 2517
- Blum, J. & Wurm, G. 2000, *Icarus*, 143, 138
- Chyba, C. F., Thomas, P. J., Brookshaw, L., & Sagan, C. 1990, *Science*, 249, 366
- Ciesla, F. J. 2010, *ApJ*, 723, 514
- Ciesla, F. J. 2011, *ApJ*, 740, 9
- Ciesla, F. J. & Cuzzi, J. N. 2006, *Icarus*, 181, 178
- Draine, B. T. 1979, *ApJ*, 230, 106
- Finocchi, F., Gail, H. P., & Duschl, W. J. 1997, *A&A*, 325, 1264
- Fomenkova, M. N. 1997, in *Astronomical Society of the Pacific Conference Series*, Vol. 122, From Stardust to Planetesimals, ed. Y. J. Pendleton, 415
- Fomenkova, M. N. 1999, *Space Sci. Rev.*, 90, 109
- Gail, H.-P. & Trieloff, M. 2017, *A&A*, 606, A16
- Gundlach, B. & Blum, J. 2015, *ApJ*, 798, 34
- Hartmann, L., Calvet, N., Gullbring, E., & D'Alessio, P. 1998, *Astrophys. J.*, 495, 385
- Hollands, M. A., Koester, D., Alekseev, V., Herbert, E. L., & Gänsicke, B. T. 2017, *MNRAS*, 467, 4970
- Homma, K. A., Okuzumi, S., Nakamoto, T., & Ueda, Y. 2019, *ApJ*, 877, 128
- Hyodo, R., Ida, S., & Guillot, T. 2021, *A&A*, 645, L9
- Ida, S. & Guillot, T. 2016, *A&A*, 596, L3
- Ida, S., Guillot, T., Hyodo, R., Okuzumi, S., & Youdin, A. N. 2021, *A&A*, 646, A13
- Ida, S., Guillot, T., & Morbidelli, A. 2016, *A&A*, 591, A72
- Ida, S., Yamamura, T., & Okuzumi, S. 2019, *A&A*, 624, A28
- Ishizaki, L., Tachibana, S., Okamoto, T., Yamamoto, D., & Ida, S. 2023, *The Astrophysical Journal*, 957, 47
- Kataoka, A., Muto, T., Momose, M., et al. 2015, *ApJ*, 809, 78
- Klarman, L., Ormel, C. W., & Dominik, C. 2018, *A&A*, 618, L1
- Koester, D. 2010, *Mem. Soc. Astron. Italiana*, 81, 921
- Koester, D., Gänsicke, B. T., & Farihi, J. 2014, *A&A*, 566, A34
- Kress, M. E., Tielens, A. G. G. M., & Frenklach, M. 2010, *Advances in Space Research*, 46, 44
- Kudo, T., Kouchi, A., Arakawa, M., & Nakano, H. 2002, *Meteoritics & Planetary Science*, 37, 1975
- Lee, J.-E., Bergin, E. A., & Nomura, H. 2010, *ApJ*, 710, L21
- Li, J., Bergin, E. A., Blake, G. A., Ciesla, F. J., & Hirschmann, M. M. 2021, *Science Advances*, 7, eabd3632
- Lichtenegger, H. I. M. & Komle, N. I. 1991, *Icarus*, 90, 319
- Matrajt, G., Muñoz Caro, G. M., Dartois, E., et al. 2005, *A&A*, 433, 979
- Musioli, G. & Wurm, G. 2019, *ApJ*, 873, 58
- Nakano, H., Kouchi, A., Tachibana, S., & Tsuchiyama, A. 2003, *ApJ*, 592, 1252
- Ohno, K. & Ueda, T. 2021, *A&A*, 651, L2
- Oka, A., Nakamoto, T., & Ida, S. 2011, *ApJ*, 738, 141
- Okamoto, T. & Ida, S. 2022, *ApJ*, 928, 171
- Okuya, A., Ida, S., Hyodo, R., & Okuzumi, S. 2023, *MNRAS*, 519, 1657
- Paquette, C., Pelletier, C., Fontaine, G., & Michaud, G. 1986, *ApJS*, 61, 177
- Ros, K., Johansen, A., Riipinen, I., & Schlesinger, D. 2019, *A&A*, 629, A65
- Saito, E. & Sironi, S.-i. 2011, *ApJ*, 728, 20
- Sakuraba, H., Kurokawa, H., Genda, H., & Ohta, K. 2021, *Scientific Reports*, 11, 20894
- Sato, T., Okuzumi, S., & Ida, S. 2016, *A&A*, 589, A15
- Savage, B. D. & Sembach, K. R. 1996, *ARA&A*, 34, 279
- Schoonenberg, D. & Ormel, C. W. 2017, *A&A*, 602, A21
- Schräpler, R. R., Landeck, W. A., & Blum, J. 2022, *MNRAS*, 509, 5641
- Ueda, T., Flock, M., & Okuzumi, S. 2019, *ApJ*, 871, 10
- Ueda, T., Tazaki, R., Okuzumi, S., Flock, M., & Sudarshan, P. 2024, *Nature Astronomy*, 8, 1148
- Wada, K., Tanaka, H., Okuzumi, S., et al. 2013, *A&A*, 559, A62
- Wada, K., Tanaka, H., Suyama, T., Kimura, H., & Yamamoto, T. 2011, *ApJ*, 737, 36
- Zsom, A., Sándor, Z., & Dullemond, C. P. 2011, *A&A*, 527, A10
- Zuckerman, B., Koester, D., Reid, I. N., & Hüensch, M. 2003, *ApJ*, 596, 477
- Zuckerman, B., Melis, C., Klein, B., Koester, D., & Jura, M. 2010, *ApJ*, 722, 725
- Zuckerman, B. & Young, E. D. 2018, in *Handbook of Exoplanets*, ed. H. J. Deeg & J. A. Belmonte (Springer International Publishing), 14

Appendix A: Tuning for a higher resolution of smaller particles

Small particles tend to be lifted up to the higher layer more easily. As discussed in Sect. 2.4.1, the mass fraction of particles smaller than $0.1 \mu\text{m}$ is given by $(0.1 \mu\text{m}/s_{\text{max}})^{0.5}$. If $s_{\text{max}} > 1 \text{ mm}$, their mass fraction is less than 1%. We assume the super-particles as aggregations of solid particles with a single size and that all super-particles have equal mass. When the mass fraction of the particles with $s \leq 0.1 \mu\text{m}$ is less than 1%, the number of super-particles should be higher than 100 to ensure the presence of the small particles. However, as shown in Eq. (28), the typical number of super-particles inside 1 au is less than 100. Thus, the probability of the super-particles with $s \leq 0.1 \mu\text{m}$ existing inside 1 au is very low.

To adjust the influence of small particles, we add ‘small’ super-particles with a fixed size of $0.1 \mu\text{m}$. These are used only for the calculation of f_c , and the Σ_d is calculated by the number of the ‘large’ super-particles alone.

In each timestep, we calculate the mass-averaged carbon fraction between the small and large super-particles given by

$$f_c = f_{c,s} \left(\frac{0.1 \mu\text{m}}{s_{\text{max}}} \right)^{0.5} + f_{c,l} \left(1 - \left(\frac{0.1 \mu\text{m}}{s_{\text{max}}} \right)^{0.5} \right), \quad (\text{A.1})$$

where $f_{c,s}$ and $f_{c,l}$ are the mass-averaged carbon fractions for small and large super-particles, respectively. We consider the redistribution of carbon between the small and large particles through coagulation and fragmentation of solids and assume that all super-particles in each bin have the average carbon fraction in the next timestep.

Appendix B: The cases of $v_{\text{frag,sil}} = v_{\text{frag,ice}}$ without the shadow area

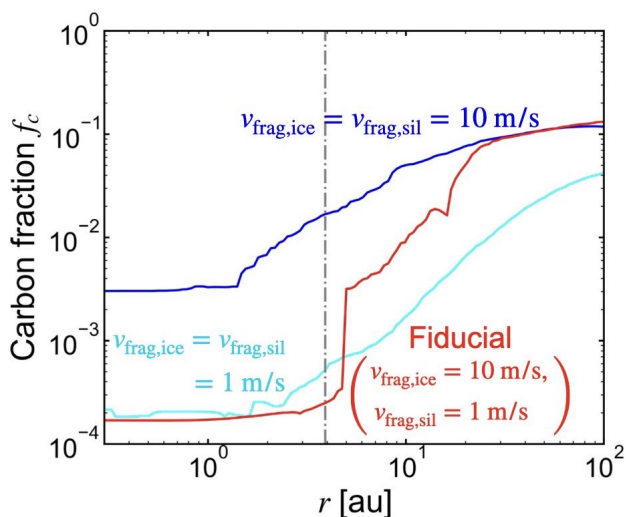


Fig. B.1: Same as Fig. 11 but without the shadow area behind the snow line.

As argued in Sect. 3.3.1, for $v_{\text{frag,sil}} = v_{\text{frag,ice}}$, the shadow area should not appear behind the snow line. Figure B.1 shows f_c at 0.68 Myr without the shadow area. The different fragmentation velocities between icy and silicate particles make a larger dichotomy in f_c between the inner and outer disk region than the other cases even if we do not consider the shadow area. The flat region in the same fragmentation velocity cases might be produced by the inefficiency of photolysis there as shown in Fig. 12.

Appendix C: Results with different parameter sets

Figure C.1 shows the time evolution of the solid surface densities (Σ_d) and f_c for different parameter sets. The times of the four lines are corresponding to the four stages discussed in Sect. 3.1. In the lower gas accretion rate stage (final stage), $\dot{M}_g = 10^{-9} M_\odot/\text{year}$, we stopped the calculation at 1 Myr, when the total solid mass inside the snow line is lower than the Earth’s mass.

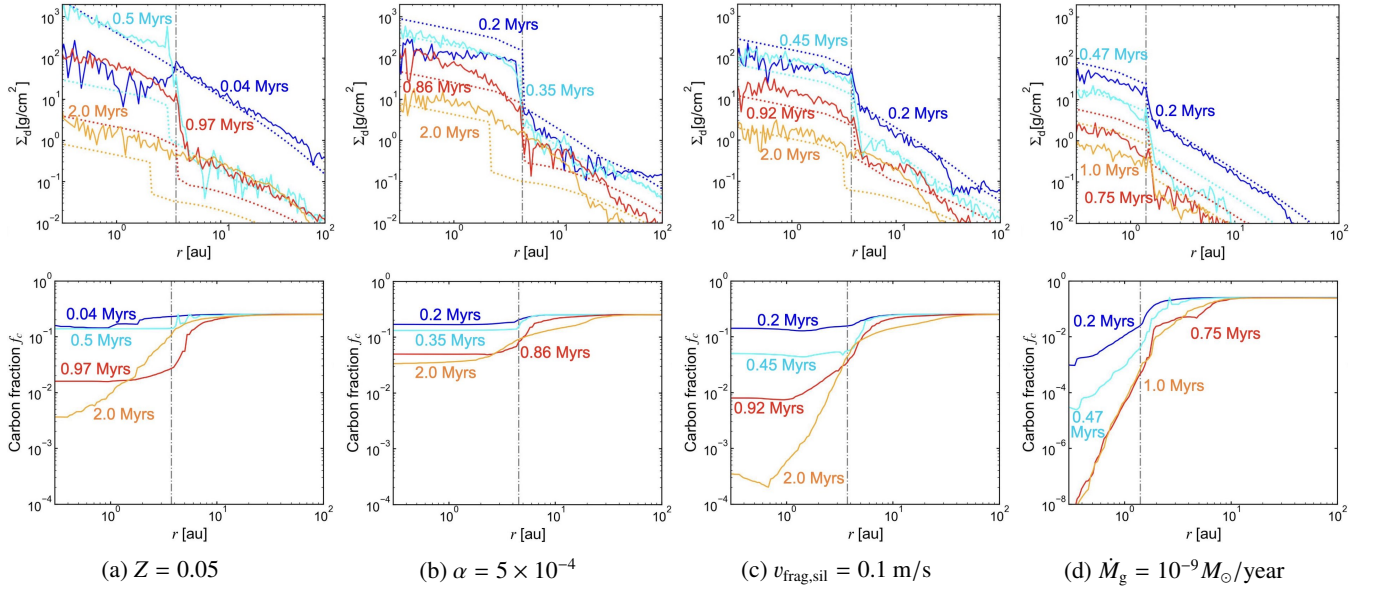


Fig. C.1: Time evolution of the solid surface densities (top row) and carbon fractions (bottom row) for each parameter set. The sub-captions show the parameter which we changed from the fiducial parameter set. The dashed lines in the top row show the analytic estimation given by Eq. 68.